Syntaxin 17 recruitment to mature autophagosomes is temporally regulated by PI4P accumulation

Authors: Saori Shinoda[1,4], Yuji Sakai[1,2], Takahide Matsui[3], Masaaki Uematsu[1,5], Ikuko Koyama-Honda[1], Jun-ichi Sakamaki[1], Hayashi Yamamoto[1,3], Noboru Mizushima[1,*]

Affiliations:

[1] Department of Biochemistry and Molecular Biology, Graduated School of Medicine, The University of Tokyo, Tokyo, Japan

[2] Department of Biosystems Science, Institute for Life and Medical Sciences, Kyoto University, Kyoto, Japan

[3] Department of Molecular Oncology, Institute for Advanced Medical Sciences, Nippon Medical School, Tokyo, Japan

[4] Present address: Faculty of Life Sciences, Kyoto Sangyo University, Kyoto, Japan

[5] Present address: Weill Institute for Cell and Molecular Biology, Cornell University, New York, USA

* Correspondence to: N. Mizushima (e-mail: nmizu@m.u-tokyo.ac.jp)

Abstract:

During macroautophagy, cytoplasmic constituents are engulfed by autophagosomes. Lysosomes fuse with closed autophagosomes but not with unclosed intermediate structures. This is achieved in part by the late recruitment of the autophagosomal SNARE syntaxin 17 (STX17) to mature autophagosomes. However, how STX17 recognizes autophagosome maturation is not known. Here, we show that this temporally regulated recruitment of STX17 depends on the positively charged C-terminal region of STX17. Consistent with this finding, mature autophagosomes are more negatively charged compared with unclosed intermediate structures. This electrostatic maturation of autophagosomes is likely driven by the accumulation of phosphatidylinositol 4-phosphate (PI4P) in the autophagosomal membrane. Accordingly, dephosphorylation of autophagosomal PI4P prevents the association of STX17 to autophagosomes. Furthermore, molecular dynamics simulations support PI4P-dependent membrane insertion of the transmembrane helices of STX17. Based on these findings, we propose a model in which STX17 recruitment to mature autophagosomes is temporally regulated by a PI4P-driven change in the surface charge of autophagosomes.

Introduction

Macroautophagy (hereafter, autophagy) is a highly conserved process of intracellular degradation (*Mizushima and Levine*, 2020; *Soreng et al.*, 2018). Membrane cisternae (called isolation membranes or phagophores) elongate, bend, and engulf cytoplasmic components. Closure of the rim of the cup-shaped structures results in the formation of autophagosomes. Subsequently, the autophagosomes fuse with lysosomes to degrade their enclosed contents. Autophagosome–lysosome fusion is strictly regulated; lysosomes fuse with only fully closed autophagosomes. If lysosomes were to fuse with intermediate unclosed structures and their inner membrane is degraded, then harmful lysosomal enzymes would leak out into the cytosol. This temporal regulation of autophagosome–lysosome fusion is achieved in mammals by two mechanisms. One is the regulated translocation of the autophagosomal SNARE syntaxin 17 (STX17), which is recruited immediately before or after the closure of autophagosomes (*Itakura et al.*, 2012; *Takáts et al.*, 2013; *Tsuboyama et al.*, 2016). The other is the activation of YKT6, a conserved autophagosomal SNARE (*Matsui et al.*, 2018), which is kept inactivated by ULK1 (a homolog of yeast Atg1)-mediated phosphorylation until the completion of autophagosome formation (ULK1/Atg1 is dissociated at this time) (*Barz et al.*, 2020; *Gao et al.*, 2020; *Sanchez-Martin et al.*, 2023). Then, STX17 interacts with SNAP29 and the lysosomal SNARE protein VAMP7 or VAMP8, and YKT6 interacts with SNAP29 and the lysosomal STX7 to mediate the fusion between autophagosomes and lysosomes.

However, the molecular mechanism underlying the late recruitment of STX17 is not known. A previous study reported that LC3/GABARAP family proteins and immunity-related GTPase M (IRGM) are involved in autophagosomal recruitment of STX17 (*Kumar et al.*, 2018a), whereas other studies have shown that LC3/GABARAP family proteins are not required (*Nguyen et al.*, 2016; *Tsuboyama et al.*, 2016). It has also been recently reported that phosphorylation of STX17 and binding to filamin A are important for STX17 recruitment (*Wang et al.*, 2023). Although these factors may help STX17 recruitment, these mechanisms do not explain the strict temporal regulation of STX17 recruitment.

Accordingly, we hypothesized that there exists a yet unknown change in some

68 autophagosomal properties during maturation that is recognized by STX17. In this
69 study, we reveal that STX17 recruitment to autophagosomes requires positively charged
70 amino acids in the C-terminal region of STX17. Consistently, autophagosomes become
71 more negatively charged when they acquire STX17. Furthermore, we show that
72 phosphatidylinositol 4-phosphate (PI4P), a negatively charged phospholipid,
73 accumulates during autophagosome maturation and is required for STX17 recruitment.
74 Based on these findings, we propose a model in which STX17 recruitment to mature
75 autophagosomes is temporally regulated by the electrostatic change of autophagosomes.
76

Results

Autophagosomal localization of STX17 requires a positively charged C-terminal region

STX17 has an N-terminal Habc domain, followed by a SNARE domain, two tandem transmembrane helices, and a short C-terminal region, with both N- and C-terminal ends facing the cytosol (Figure 1A) (*Itakura et al.*, 2012). A short construct containing only the transmembrane helices and the C-terminal region (STX17TM), which behaves similarly to full-length STX17 (*Itakura et al.*, 2012), colocalized with ring-shaped autophagosomes labeled with the general autophagic membrane marker microtubule-associated protein light chain 3B (LC3B) (Figure 1B and C). STX17 is a tail-anchored protein, and the C-terminal region of tail-anchored proteins is generally important for specific membrane targeting (*Rao et al.*, 2016; *Yagita et al.*, 2013). Therefore, we determined the role of the C-terminal region of STX17. In the following experiments, we used the STX17TM construct in order to avoid detecting an indirect effect of SNARE domain-mediated translocation. Deletion of the C-terminal cytosolic region from STX17TM (TMΔC) resulted in a diffuse cytosolic pattern (Figure 1C), indicating that not only the transmembrane helices but also the C-terminal region of STX17 are required for its proper autophagosomal localization. Although the role of STX17 in autophagosome–lysosome fusion is conserved in both *Drosophila melanogaster* (Dm) (*Takáts et al.*, 2013) and *Caenorhabditis elegans* (Ce) (*Guo et al.*, 2014), the amino acid sequence of the C-terminal region is not conserved in these organisms (Figure 1—figure supplement 1A). Nevertheless, when expressed in mammalian cells, DmSTX17TM and CeSTX17TM were recruited to autophagosomes, although less efficiently (Figure 1—figure supplement 1B), suggesting that recruitment of STX17 does not depend on the specific amino acid sequence in the C-terminal region.

In general, cationic amino acids in the C-terminal region of tail-anchored proteins are important for targeting membranes (*Borgese et al.*, 2001; *Horie et al.*, 2002; *Yagita et al.*, 2013). STX17 has cationic amino acids in its C-terminal region, and the replacement of lysine and arginine with alanine impaired autophagosomal localization in a dose-dependent manner (Figure 1A and D, Figure 1—figure supplement 1C).

Moreover, the replacement of the C-terminal region with artificial sequences consisting of five residues of positively charged lysine or arginine, but not negatively charged aspartic acid or uncharged alanine, restored the localization of STX17 to autophagosomes (Figure 1E, Figure 1—figure supplement 1D). These data suggest that autophagosomal localization of STX17 requires positively charged residues, but not sequence-specific structures, in its C-terminal region.

Autophagosomes become negatively charged during maturation

Given the importance of positively charged residues in the C-terminal region, we hypothesized that STX17 favors negatively charged membranes. To evaluate this hypothesis, we first conducted an *in vitro* membrane binding assay using liposomes with different compositions of phospholipids. STX17 was efficiently recruited to liposomes containing anionic phospholipids such as phosphatidylserine (PS), phosphatidylinositol 3-phosphate (PI3P) or PI4P (Figure 2A). These data suggest that STX17 can be recruited to negatively charged membranes independent of the specific lipid species.

Next, we tested whether autophagosomal membranes are indeed negatively charged. To monitor membrane charge *in vivo*, we used membrane surface charge biosensors (Figure 2B) (*Simon et al.*, 2016; *Yeung et al.*, 2006). These surface charge probes have a diverse range of positively charged peptides and a farnesylated anchor at their C terminus, with GFP fused to their N terminus. The name of each probe is indicated by the number of positively charged amino acids (lysines) followed by that of negatively charged amino acids (glutamines). The probe for the most negatively charged membrane (9K0Q) labeled the plasma membrane, which is known to have a highly negative charge (*Li et al.*, 2014), but not autophagosomes (Figure 2C and D, Figure 2—figure supplement 1A). However, the probes for intermediate (5K4Q and 3K6Q) and weakly (1K8Q) negative charges labeled not only the plasma membrane but also LC3B- and STX17-positive autophagosomes (Figure 2C and D, Figure 2—figure supplement 1A). The recruitment kinetics differed between the intermediate and weakly negative charge probes. The 1K8Q probe was recruited to not only STX17-positive spherical autophagosomes but also STX17-negative, LC3B-positive elliptic structures that should correspond to unclosed autophagosomes (*Tsuboyama et al.*, 2016) (Figure 2E). In

139 contrast, the intermediate charge probes (3K6Q and 5K4Q) were recruited to spherical
140 LC3B-positive autophagosomes at almost the same time as STX17 (Figure 2F, Figure
141 2—figure supplement 1B). Structures positive for ATG5, a marker for unclosed
142 autophagosomes, were labeled with 1K8Q but not with 3K6Q or 5K4Q (Figure 2F,
143 Figure 2—figure supplement 1C). These results, which are summarized in Figure 2G,
144 suggest that mature autophagosomes are more negatively charged compared with
145 unclosed intermediate structures.
146
147 **The accumulation of PI4P in mature autophagosomes coincides with STX17**
148 **recruitment**
149 We next explored the mechanism that generates the negative charges of autophagosomal
150 membranes. As the change in the membrane charge was rapid and robust, we reasoned
151 that it could be caused by a change in lipid composition or modification. We screened
152 negatively charged lipids that are enriched in autophagosomal membranes using various
153 phospholipid probes (*Platre and Jaillais*, 2016). Among them, we found that the probes
154 for PI4P (GFP-fused PH domain of CERT; GFP–CERT(PHD) and phosphatidylinositol
155 3,5-bisphosphate (PI(3,5)P_2) (GFP–TRPML1(PHD)) colocalized with STX17-positive
156 ring-shaped structures (Figure 3—figure supplement 1A). Since PI(3,5)P_2 was primarily
157 present in lysosomes (Figure 3—figure supplement 1B) (*Dong et al.*, 2010), PI(3,5)P_2
158 enrichment likely occurs after fusion with lysosomes. Consistently, other PI4P probes,
159 including FAPP(PHD), OSBP(PHD), and P4M-SidMx2, colocalized with STX17TM
160 (Figure 3—figure supplement 2A and B) (*Hammond et al.*, 2014; *Platre and Jaillais*,
161 2016).
162 PI4P is an important lipid component of the Golgi complex and the plasma
163 membrane as well as a major regulator of conserved eukaryotic cellular processes
164 (*Balla*, 2013; *Platre et al.*, 2018; *Schink et al.*, 2016). In the context of autophagy, it was
165 previously reported that GABARAP-dependent PI4P production by PI4K2A (PI4KIIα)
166 is required for autophagosome–lysosome fusion (*Wang et al.*, 2015), and that PI4KB
167 (PI4KIIIβ) is detected in ATG9A vesicles and early autophagic structures and is
168 furthermore required for autophagosome formation (*Judith et al.*, 2019). Consistently,
169 we detected faint signals of PI4K2A and PI4KB on LC3B-positive structures (Figure

170 3—figure supplement 1C). However, the dynamics of PI4P production during
171 autophagosome maturation has not been systematically determined.
172 The PI4P probes (CERT(PHD), FAPP(PHD), OSBP(PHD), and P4M-SidMx2)
173 colocalized with STX17 but not with ATG5 (Figure 3A, Figure 3—figure supplement
174 2A and B), suggesting that PI4P accumulates in mature autophagosomes. We then
175 investigated the dynamics of PI4P enrichment by time-lapse microscopy. The signal of
176 the CERT(PHD) probe appeared on LC3B-positive membranes only after the
177 disappearance of the unclosed autophagosome markers ATG5 and WIPI2B (Figure 3B
178 and C) and almost at the same time as STX17 localized (Figure 3D). This was followed
179 by the appearance of LysoTracker signals (note that LysoTracker signals have been
180 previously observed to appear ring-shaped until inner membrane degradation
181 (*Tsuboyama et al.*, 2016)) (Figure 3—figure supplement 2C). To confirm that PI4P
182 accumulation was independent of autophagosome–lysosome fusion, we evaluated the
183 colocalization among the PI4P probe, LC3B, and LAMP1 in STX17- and YKT6-
184 double-knockdown cells, in which unfused autophagosomes accumulated (*Matsui et al.*,
185 2018). The punctate structures of CERT(PHD) were still colocalized with LC3B-
186 positive and LAMP1-negative structures in these double-knockdown cells (Figure 3—
187 figure supplement 2D). These results suggest that PI4P accumulates in mature
188 autophagosomal membranes independent of lysosome fusion and that the kinetics of the
189 accumulation of STX17, the PI4P probes, and the negative charge probes are associated.
190
191 **STX17 recruitment to autophagosomes depends on PI4P**
192 To determine whether PI4P is required for the recruitment of STX17 to
193 autophagosomes, we first tried to dephosphorylate PI4P by ectopic expression of SAC1,
194 a PI4P-phosphatase, on autophagosomes (*Manford et al.*, 2010). To this end, we fused
195 the phosphatase domain of yeast Sac1 (Sac1PD) to the N terminus of LC3B and
196 expressed them in different cell lines, using several methods, including lipofection and
197 retrovirus- and adenovirus-mediated transfection. Although Sac1PD–LC3B localized to
198 autophagosomes, it did not reduce either the level of autophagosomal PI4P or STX17
199 recruitment (unpublished observation). High expression of Sac1PD–LC3B inhibited
200 autophagosome formation (unpublished observation). Mammals possess four PI 4-

kinases. We next tried to deplete each or combinations of these PI 4-kinases by using siRNA or an auxin-inducible degron system (*Yesbolatova et al.*, 2020) or inhibit them using PI 4-kinase inhibitors, including PI-273 (*Li et al.*, 2017), BF738735 (*van der Schaar et al.*, 2013), and NC03 (*Sengupta et al.*, 2019), but ultimately failed to reduce the autophagosomal PI4P levels and STX17 recruitment (unpublished observation). Although the precise reason for this failure was not known, these approaches were insufficient to deplete autophagosomal PI4P *in vivo*.

Therefore, we instead used an *in vitro* system to determine whether PI4P is important for STX17 recruitment to autophagosomes (Figure 4A). Mature autophagosomes prior to fusion with lysosomes were isolated from *STX17* knockout (KO) cells (Figure 4B, Fraction #1) (*Matsui et al.*, 2018). Recombinant Sac1PD, its phosphatase-dead mutant (C392S), and mGFP–STX17TM were generated using insect cells (Figure 4C). Autophagosomes were first incubated with or without Sac1PD or Sac1PD (C392S) for 30 min and then further incubated with mGFP–STX17TM for another 30 min. Recombinant mGFP–STX17TM was associated with autophagosomes, but it was significantly impaired by treatment with Sac1PD. Phosphatase-dead Sac1PD (C392S) showed no effect (Figure 4D). These data suggest that PI4P is important for autophagosomal recruitment of STX17.

We further determined the effect of PI4P on the dynamics of STX17TM on a membrane by performing a molecular dynamics simulation. We used all-atom models for STX17TM and the highly mobile membrane-mimetic (HMMM) model for the lipid bilayer (*Ohkubo et al.*, 2012). The structure of STX17TM was predicted by trRosetta (*Du et al.*, 2021), yielding five different models, all of which were used in the simulation. The initial configuration was prepared such that the center of mass of STX17TM was located 3 nm above the membrane surface, after which the movement of STX17TM was tracked. In independent simulations using four out of the five predicted STX17TM structures, STX17TM was inserted into the membrane with PI4P (PC:PE:PI4P = 70:20:10) within a short time scale of 100 ns (Figure 5A, B, Video 1). The two transmembrane helices were inserted into the membrane, while the charged C-terminal region remained bound to the membrane surface (Video 1). In contrast, STX17 diffused freely in the solution and was not inserted into the membrane without PI4P

232 (PC:PE = 70:30) in simulations of all five structures (Figure 5C, D, Video 2). These
233 results suggest that STX17TM can be readily inserted into PI4P-containing membranes.
234

Discussion

Based on the results of this study, we propose a model in which temporally regulated autophagosome–lysosome fusion involves a dynamic change in electrostatic status during autophagosome maturation; the recruitment of STX17 to mature autophagosomes is primarily mediated by the electrostatic interaction between the positively charged C-terminal region of STX17 and negatively charged autophagosomal membranes (Figure 5E). Because STX17 does not localize to all negatively charged membranes (e.g., the plasma membrane), the transmembrane helices appear to also regulate the specificity of target membranes. This is consistent with the "coincidence detector" mechanism in which both a cationic motif and a nearby membrane-anchored moiety are important for membrane targeting (*Carlton and Cullen*, 2005; *Yeung and Grinstein*, 2007).

A striking finding of this study is that autophagosomes become more negatively charged during maturation, most likely through an increase in the PI4P content of their membranes, although we do not exclude the possible involvement of other negatively charged molecules. While PI3P is important for autophagosome formation, we do not think that PI3P contributes to the increase in negative charge. It was reported that PI3P is dephosphorylated to PI during autophagosome formation or maturation (*Allen et al.*, 2020; *Cebollero et al.*, 2012; *Taguchi-Atarashi et al.*, 2010), and that the PI3P effectors DFCP1 and WIPI family proteins are not detected on mature autophagosomes (*Koyama-Honda et al.*, 2013). In fact, we did not detect WIPI2B and the PI3P reporter GFP–2×FYVE on PI4P-enriched structures (Figure 3C) and STX17-positive structures (Figure 3—figure supplement 1A), respectively. Considering the change in autophagosomal membrane charge, the amount of PI4P produced during autophagosome maturation is likely to be higher than that of PI3P in the early stages. Surface charge, which is now recognized as one of the key physical properties of cellular membranes, regulates various biological processes (*Yeung and Grinstein*, 2007). For example, the negatively charged plasma membrane, where anionic phospholipids such as PI(4,5)P_2 and PS are enriched, recruits positively charged proteins, including K-Ras and Rac1 (*Bigay and Antonny*, 2012; *Heo et al.*, 2006; *Li et al.*, 2014; *Platre et al.*,

266 2018; *Yeung et al.*, 2008; *Yeung et al.*, 2006), some of which are released from the
267 membrane when the negative charge of the surface is reduced during phagocytosis
268 (*Yeung et al.*, 2006). However, little has been reported on the role of electrostatic
269 properties of other organelles, including autophagosomes.
270 PI4P is involved in many cellular processes, including autophagosome
271 formation and maturation. It was reported that PI4KB regulates the early stage of
272 autophagosome formation through interaction with ATG9A (*Judith et al.*, 2019). It was
273 also reported that PI4K2A is recruited to autophagosomes by binding to the ATG8
274 family proteins GABARAP and GABARAPL1 and produces PI4P in the
275 autophagosomal membranes (*Wang et al.*, 2015). Furthermore, the knockdown of
276 PI4K2A resulted in the accumulation of abnormally enlarged autophagosomes,
277 presumably owing to a defect in autophagosome–lysosome fusion (*Wang et al.*, 2015).
278 Indeed, a freeze-fracture replica labeling study showed that autophagosomal membranes
279 contain PI4P in the cytoplasmic leaflets of the outer and inner membranes (*Kurokawa et*
280 *al.*, 2019). Very recently, it was reported that the knockdown of PI4KIIα in *Drosophila*
281 blocked autophagic flux at a late step of autophagy in the fat body (*Liu et al.*, 2023).
282 Although these studies are consistent with our finding that PI4P production induces
283 STX17 recruitment for fusion with lysosomes, our repeated attempts to deplete PI4P
284 genetically (i.e., by depletion of PI 4-kinases or attachment of Sac1 to autophagosomes)
285 or pharmacologically did not deplete autophagosomal PI4P or inhibit STX17
286 recruitment. Liu et al. also showed that the knockdown of PI4KIIα in *Drosophila* did
287 not inhibit STX17 recruitment. This may be because PI 4-kinases function redundantly.
288 Generally, PI4P can be structurally recognized by a series of PI4P-binding
289 domain-containing proteins (*Lemmon*, 2008; *Moravcevic et al.*, 2012). However, recent
290 studies also suggest that PI4P can generate a negatively charged electrostatic field
291 (*Hammond et al.*, 2012; *Simon et al.*, 2016). In such cases, positively charged proteins
292 can be recruited independent of specific amino acid motifs. Examples of the role of
293 PI4P in electrostatic signature include the recruitment of the polar auxin transport
294 regulator PINOID and other signaling molecules to the cell plate in plants (*Simon et al.*,
295 2016); the recruitment of D6 protein kinase (*Barbosa et al.*, 2016), NPH3 (*Reuter et al.*,
296 2021), and the exocyst complex (*Synek et al.*, 2021) to the plasma membrane in plants;

297 the recruitment of Lgl and Dlg proteins, which function in cell polarity and
298 tumorigenesis, to the plasma membrane in *Drosophila* (*Dong et al.*, 2015; *Lu et al.*,
299 2021); and the recruitment of NLRP3 to the disassembled trans-Golgi network during
300 inflammasome activation in mammals (*Chen and Chen*, 2018). In the present study, we
301 showed that autophagosomal PI4P also serves as a regulator of surface charge. Given
302 that the function of elongating unclosed autophagosomes (i.e., sequestration) and
303 mature closed autophagosomes (i.e., fusion with lysosomes) differs despite using
304 seemingly the same membrane, electrostatic maturation would be an efficient way for
305 the function to switch.
306
307

Materials and Methods

Plasmids and antibodies

First, cDNAs encoding human STX17 (*Itakura et al.*, 2012), *D. melanogaster* STX17 (NM_079202), *C. elegans* STX17 (NM_059941), rat LC3B (*Hara et al.*, 2008), and mouse ATG5 (NM_053069) were inserted into pMRXIP (harboring a puromycin-resistant marker) (*Kitamura et al.*, 2003; *Saitoh et al.*, 2002), pMRXIZ (harboring a zeocin-resistant marker) (*Morita et al.*, 2018), and pMRXIB (harboring a blasticidin-resistant marker) (*Morita et al.*, 2018) together with enhanced GFP or mRuby3 (codon-optimized, Addgene #74252). STX17 fragments and their point mutations were generated by a standard PCR method or PCR-mediated site-directed mutagenesis.

Membrane surface charge probes were constructed by annealing with the following oligonucleotides (purchased from Thermo Fisher Scientific), after which they were inserted into pMRXIP plasmid with enhanced GFP:

GFP–9K0Q (GGCTCGGGATCCGGGAATTCATCCAAAGATGGAAAAAAAAAGAAGAAGAAAAGTAAAACCAAATGCGTGATTATGTAACTCGAGAGCGGCCGCT, AGCGGCCGCTCTCGAGTTACATAATCACGCATTTGGTTTTACTTTTCTTCTTCTTTTTTTTCCATCTTTGGATGAATTCCCGGATCCCGAGCC); GFP–5K4Q (GGCTCGGGATCCGGGAATTCAAGCAAAGACGGCCAGCAGCAACAAAAGAAGTCTAAGACCAAGTGTGTAATCATGTAACTCGAGAGCGGCCGCT, AGCGGCCGCTCTCGAGTTACATGATTACACACTTGGTCTTAGACTTCTTTTGTTGCTGCTGGCCGTCTTTGCTTGAATTCCCGGATCCCGAGCC); GFP–3K6Q (GGCTCGGGATCCGGGAATTCATCCAAGGACGGACAACAGCAGCAACAACAGAGTAAAACTAAATGCGTGATAATGTAACTCGAGAGCGGCCGCT, AGCGGCCGCTCTCGAGTTACATTATCACGCATTTAGTTTTACTCTGTTGTTGCTGCTGTTGTCCGTCCTTGGATGAATTCCCGGATCCCGAGCC); GFP–1K8Q (GGCTCGGGATCCGGGAATTCATCCCAGGACGGTCAGCAGCAACAACAGCAATCACAAACTAAATGTGTAATAATGTAACTCGAGAGCGGCCGCT, AGCGGCCGCTCTCGAGTTACATTATTACACATTTAGTTTGTGATTGCTGTTGTTGCTGCTGACCGTCCTGGGATGAATTCCCGGATCCCGAGCC). GFP-0K9Q was

generated by PCR-mediated site-directed mutagenesis.

To generate lipid probes, cDNAs encoding human 2×Spo20(PABD) (NM_005633; amino acids 422–551) (*Kassas et al.*, 2017), CERT(PHD) (NM_001130105; amino acids 1–116) (*Hanada*, 2006), FAPP (NM_001807; amino acids 1–101) (*Balla et al.*, 2005), OSBP (NM_002556; amino acids 87–185) (*Levine and Munro*, 1998), 2×ING2(PlantHD) (NM_001564; amino acids 190–280) (*Gozani et al.*, 2003), 2×TAPP1(PHD) (NM_001001974; amino acids 184–304) (*Dowler et al.*, 2000), 2×TRPML1(PHD) (NM_020533; amino acids 1–69) (*Dong et al.*, 2010), Btk (NM_000061; amino acids 1–177) (*Baraldi et al.*, 1999), and rat PLCd1 (NM_017035; amino acids 1–175) (*Varnai and Balla*, 1998) were inserted into pMRXIP. GFP–Evectin-2 was provided by Hiroyuki Arai; GFP–PKD C1ab was provided by Tamas Balla; and mRFP–2×FYVE was provided by Harald Stenmark. GFP–P4M-SidMx2 (51472; Addgene) was amplified by PCR and subcloned into pMRXIP.

For the *in vitro* autophagosome recruitment assay, DNA fragments encoding GST–HRV3C-tagged yeast Sac1 (phosphatase domain; 2–517 amino acids) (NM_001179777) or its C392S mutant and mGFP (monomeric enhanced GFP with A206K mutation)–STX17TM were inserted downstream of the polyhedrin promoter of the pFastBac Dual Expression vector (10712024; Thermo Fisher Scientific).

For immunoblotting, mouse monoclonal anti-TOMM20 (sc-11415; Santa Cruz Biotechnology, Inc.), rabbit polyclonal anti-LAMP1 (ab24170; Abcam), anti-p62 (PM045; MBL), and anti-LC3B (*Kabeya et al.*, 2000) antibodies were used as primary antibodies. HRP-conjugated anti-mouse IgG and HRP-conjugated anti-rabbit IgG (111-035-003, 111-035-144; Jackson ImmunoResearch Laboratories) antibodies were used as secondary antibodies.

For immunostaining, rabbit polyclonal anti-LAMP1 (ab24170; Abcam) was used as a primary antibody, while Alexa Fluor 660-anti-rabbit IgG (A-21074; Molecular Probes) was used as secondary antibodies.

Cell culture

Mouse embryonic fibroblasts (MEFs), U2OS cells, HeLa cells, and human embryonic kidney (HEK) 293T cells were cultured in Dulbecco's modified Eagle's medium

370 (DMEM) (D6546; Sigma-Aldrich) supplemented with 10% fetal bovine serum (FBS)
371 (S1820500; Biowest) and 2 mM L-glutamine (25030081; Gibco) in a 5% CO_2 incubator.
372 For the starvation treatment, cells were washed twice with phosphate-buffered saline
373 (PBS) and incubated in amino acid-free DMEM (04833575; Fujifilm Wako Pure
374 Chemical Corp.) without FBS. The *STX17* KO HeLa cells used in the present study
375 were as previously described(*Matsui et al.*, 2018).
376
377 **Retroviral infections and generation of stable cell lines**
378 HEK293T cells were transiently transfected using Lipofectamine 2000 (11668019;
379 Thermo Fisher Scientific) or Fugene HD (VPE2311; Promega) with retrovirus vectors,
380 pCG-gag-pol, and pCG-VSV-G (provided by Teruhiko Yasui). After cells were cultured
381 for 2–3 days, the supernatant was collected and filtered through a 0.45-μm syringe filter
382 unit (SLHV033RB; EMD Millipore). The obtained cells were cultured with retrovirus
383 and 8 μg/ml polybrane (H9268; Sigma-Aldrich). Uninfected cells were eliminated by
384 puromycin (P8833; Sigma-Aldrich), blasticidin (02218713; Fujifilm Wako Pure
385 Chemical Corp.), geneticin (10131; Thermo Fisher Scientific), and zeocin (R25005;
386 Thermo Fisher Scientific).
387
388 **Fluorescence microscopy**
389 Live-cell fluorescence imaging was performed using a Delta Vision Elite widefield
390 fluorescence microscope (GE Healthcare Life Science) equipped with a 100× PlanAPO
391 oil-immersion objective lens (Olympus, NA1.40) and a cooled-CCD camera
392 (Photometrics, CoolSNAP HQ2). Cells stably expressing GFP and mRuby3 were grown
393 on a glass-bottom dish (617870; Greiner bio-one, or 11004006; IWAKI). To observe
394 lysosomes, 50 nM Lysotracker Red DND99 (L7528; Thermo Fisher Scientific) or
395 LysoTracker Deep Red (L12492; Thermo Fisher Scientific) was added to the medium.
396 To observe HaloTag–LC3B, cells were observed in the presence of 200 nM SaraFluor
397 650T HaloTag ligand (GoryoChemical, A308-02). During live-cell imaging, the culture
398 dish was mounted in a chamber (INUB-ONI-F2; TOKAI HIT) to maintain the culture
399 conditions (37°C, 5% CO_2). Images were acquired at 30-s intervals. Time series of 16-
400 bit images were converted into RGB Tiff images using ImageJ software (Rasband, W.S.,

401 ImageJ, U. S. National Institutes of Health, http://imagej.nih.gov/ij/, 1997–2018). GFP
402 intensity of autophagosomal structures was determined using ImageJ. Additionally,
403 mRuby3–LC3 or Atg5-positive structures, including punctate and cup-shape structures
404 (premature autophagosomes) and ring-like structures (mature autophagosomes) were
405 extracted by the Analyze Particle function after binarization using the Auto Threshold
406 v1.17 plugin (Method, Max Entropy). The GFP intensity of each particle was measured
407 by the Measure ImageJ plugin, and the background signal (i.e., average GFP intensity of
408 the entire cell) was subtracted.
409 The GFP–STX17TM intensity of mature autophagosomes or liposomes was
410 determined using ImageJ. The center of ring-like structures in the red channel (LC3B or
411 liposome signals) was first selected using the multi-point tool. The region of interest
412 (ROI) was then defined by drawing a 10-μm-diameter circle around the previously
413 determined center and capturing thered channel (LC3B or liposome signals). The GFP–
414 STX17TM intensity was measured by the Radial Profile Plot ImageJ plugin, and the
415 background signal of the surrounding cytosol area was subtracted.
416
417 **Preparation of recombinant proteins**
418 *In vitro* transcription and translation in the rabbit reticulocyte lysate system were
419 performed according to a published method with minor modifications (*Sharma et al.*,
420 2010). For *in vitro* mRNA synthesis, DNA templates containing the SP6 RNA
421 polymerase promoter site upstream of the sequence to be transcribed were generated by
422 a standard PCR method and then incubated for 1 h at 37°C using the mMACHINE SP6
423 Transcription Kit (AM1340; Thermo Fisher Scientific). For *in vitro* protein synthesis,
424 transcripts were incubated with rabbit reticulocyte lysates (L4960; Promega) for 30 min
425 at 37°C.
426 Recombinant yeast Sac1 (amino acids 2–517) and mGFP–STX17TM (amino
427 acids 229–302) proteins were prepared using the Bac-to-Bac baculovirus expression
428 system (10359016; Thermo Fisher Scientific). Bacmid DNAs were prepared using
429 DH10Bac *E. coli* cells (10361012; Thermo Fisher Scientific), after which High Five
430 insect cells (BTI-TN-5B1-4; B85502; Thermo Fisher Scientific) were transfected with
431 the bacmid DNAs using Cellfectin II (10362100; Thermo Fisher Scientific).

432 Baculoviruses were generated and amplified in the High Five cells. After a 96-h viral
433 infection, the cells were suspended in 2 ml of ice-cold homogenization buffer (20 mM
434 HEPES-KOH, pH 7.2, 250 mM sucrose, 1 mM EDTA, and protease inhibitor cocktail).
435 Cells were then disrupted by ultrasonication using a UD-201 ultrasonic disruptor
436 (TOMY). After centrifugation at 16,500 × *g* for 10 min, the supernatants were incubated
437 with Glutathione Sepharose 4B (17075601; GE Healthcare) for 3 h at 4°C with gentle
438 rotation. The sepharose resins were washed three times with homogenization buffer and
439 then treated with HRV3C protease (206-18151; Fujifilm Wako Pure Chemical Corp.) for
440 12 h at 16°C. The eluted proteins were stored at −80°C. To confirm recombinant
441 expression, purified samples were separated by SDS-PAGE and detected by CBB
442 staining using CBB Stain One Super (11642-31; Nacalai Tesque).
443
444 **Preparation of phospholipid vesicles**
445 Liposomes were prepared as follows. First, 1,2-dioleoyl-sn-glycero-3-phosphocholine
446 (DOPC) (850375 C; Avanti Polar Lipids), 1,2-dioleoyl-sn-glycero-3-
447 phosphoethanolamine (DOPE) (850725 C; Avanti Polar Lipids), 1,2-dioleoyl-sn-
448 glycero-3-phospho-L-serine (DOPS) (840035P; Avanti Polar Lipids), 1,2-dioleoyl-sn-
449 glycero-3-phospho-(1′-myo-inositol) (18:1 PI) (850149P; Avanti Polar Lipids), 1,2-
450 dioleoyl-sn-glycero-3-phospho-(1′-myo-inositol-3′-phosphate) (18:1 PI3P) (850150P;
451 Avanti Polar Lipids), 1,2-dioleoyl-sn-glycero-3-phospho-(1′-myo-inositol-4′-phosphate)
452 (18:1 PI4P) (850151P; Avanti Polar Lipids), and 1,2-dioleoyl-sn-glycero-3-phospho-(1′-
453 myo-inositol-3′,4′-bisphosphate) (18:1 PI(3,4)P_2) (850153P; Avanti Polar Lipids)
454 dissolved in chloroform to 1 μM final concentrations were mixed in a glass tube at the
455 indicated ratios in the figure legends. Then, 1,2-distearoyl-sn-glycero-3-
456 phosphoethanolamine-*N*-[biotinyl(polyethylene glycol)-2000] (DSPE-PEG(2000)
457 Biotin) (880129C; Avanti Polar Lipids) and 1,2-dioleoyl-sn-glycero-3-
458 phosphoethanolamine-*N*-(lissamine rhodamine B sulfonyl) (18:1 Liss Phod PE)
459 (810150C; Avanti Polar Lipids) were added to the mixtures to label the liposomes. The
460 chloroform was evaporated under argon gas and then completely dried in a vacuum
461 desiccator overnight. The lipid film was hydrated in KHM buffer (20 mM HEPES-
462 NaOH [pH 7.4], 110 mM potassium acetate, 2 mM $MgCl_2$) at a concentration of 1 mM

463 and incubated for 16 h at 30°C.
464
465 **Purification of mature autophagosomes**
466 *STX17* KO HeLa cells stably expressing mRuby3–LC3B were harvested from two 10-
467 cm dishes and washed twice with ice-cold PBS. The cell pellets were collected after
468 centrifugation at 700 × *g* for 5 min and resuspended in 1 ml of ice-cold homogenization
469 buffer (20 mM HEPES-KOH, pH7.2, 250 mM sucrose, 1 mM EDTA, and protease
470 inhibitor cocktail). Cells were then disrupted by passage through a 25-gauge needle. The
471 homogenized cells were centrifuged at 3,000 × *g* for 10 min to remove cell debris and
472 undisrupted cells. The supernatant was diluted with an equal volume of 50% OptiPrep
473 (1893; Cosmo Bio) with complete EDTA-free protease inhibitor (11873580001; Roche).
474 Discontinuous OptiPrep gradients were generated in MLS-50 tubes (344057; Beckman
475 Coulter) by overlaying each of the following OptiPrep solutions in homogenization
476 buffer (20 mM HEPES-KOH [pH 7.4], 250 mM sucrose, 1 mM EDTA): 1.25 ml of the
477 diluted supernatant in 25% OptiPrep, 0.25 ml in 20%, 0.75 ml in 15%, 0.75 ml in 10%,
478 2.0 ml in 5%, and 0.25 ml in 0%. The gradients were centrifuged at 150,000 × *g* in
479 MLS-50 rotors (Beckman Instruments) for 3 h, and subsequently, 10 fractions (0.5 ml
480 each) were collected from the top. Proteins in each fraction were isolated by TCA
481 precipitation. The samples were separated by SDS-PAGE and transferred to Immobilon-
482 P polyvinylidene difluoride membranes (IPVH00010; EMD Millipore). Immunoblotting
483 analysis was performed with the indicated antibodies. Immobilon Western
484 Chemiluminescent HRP Substrate (P90715; EMD Millipore) was used to visualize the
485 signals, which were detected on an IQ800 biomolecular imager (Cytiva). Contrast and
486 brightness adjustments were performed using Photoshop 2022 (Adobe).
487
488 ***In vitro* recruitment assay**
489 For the liposome binding assay, the prepared liposomes were mixed with recombinant
490 proteins produced by rabbit reticulocyte lysate for 15 min at 30°C. A 0.2-mm-thick
491 chamber was created by attaching two glass cover slips (Matunami glass) together with
492 double-sided tape applied along the long edges. NeutrAvidin Protein (31000; Thermo
493 Fisher Scientific) was added to the chamber for 15 min at room temperature before

494 being washed out with KHM buffer. The liposome–recombinant protein mixture was
495 then transferred to the NeutrAvidin Protein-coated chamber. Images were captured
496 immediately after using a confocal microscope (FV3000; Olympus) equipped with a
497 60× PlanAPO oil-immersion objective lens (Olympus, NA1.42).
498 For the autophagosome recruitment assay, the LC3-positive, LAMP1-negative
499 autophagosomal fraction was incubated with 0.5 μg of Sac1 proteins from insect cells
500 for 30 min at 37°C. Then, mGFP–STX17TM was added to the mixture, which was then
501 incubated again for 30 min at 37°C. The mixtures were transferred to a glass-bottom
502 dish (617870; Greiner bio-one), and images were captured using a fluorescence
503 microscope (BZ-810; Keyence) equipped with a 60× oil-immersion objective lens
504 (Nikon, NA1.40).
505
506 **RNA interference**
507 Stealth RNAi oligonucleotides were purchased from Thermo Fisher Scientific. The
508 following sequences were used: human YKT6 siRNA antisense, 5′-
509 GGTGTGGTCATTGCTGACAATGAAT -3′; human YKT6 siRNA antisense sense, 5′-
510 ATTCATTGTCAGCAATGACCACACC -3′ (*Matsui et al.*, 2018). The siRNA
511 oligonucleotides for human STX17 (HSS123732 antisense, 5′-
512 AATTAAGTCCGCTTCTAAGGTTTCC -3′; HSS123732 sense, 5’-
513 GGAAACCTTAGAAGCGGACTTAATT -3′) were previously reported (*Itakura et al.*,
514 2012). The stealth RNAi oligonucleotides were transfected into cells using
515 Lipofectamine RNAiMAX (13778150; Thermo Fisher Scientific) according to the
516 manufacturer’s instructions. Three days after transfection, cells were used for analysis.
517
518 **Immunostaining**
519 Cells grown on coverslips were washed with PBS and fixed with 4% paraformaldehyde
520 phosphate buffer solution (0915485; Nacalai Tesque) for 10 min at room temperature.
521 Fixed cells were permeabilized with 50 μg/ml digitonin (D141; Sigma-Aldrich) in PBS
522 for 5 min, blocked with 3% BSA in PBS for 10 min, and then incubated with primary
523 antibodies for 16 h at 4°C. After being washed three times with PBS, cells were
524 incubated with secondary antibodies for 1 h at room temperature. The coverslips were

525 observed using a confocal laser microscope (FV3000; Olympus) equipped with a 60×
526 PlanAPO oil-immersion objective lens (Olympus, NA1.42).
527
528 **Sequence alignment**
529 Amino acid sequences of STX17 from the following species were obtained from the
530 NCBI protein database: *Homo sapiens* (NP_060389.2), *Mus musculus* (NP_080619.2),
531 *Danio rerio* (NP_001007450.1), *Ciona intestinalis* (NP_492342.1), *Drosophila*
532 *melanogaster* (NP_523926.1), and *Caenorhabditis elegans* (NP_492342.1). The
533 sequences were aligned using clustal W (https://www.genome.jp/tools-bin/clustalw) as
534 implemented in Molecular Evolutionary Genetics Analysis X (*Kumar et al.*, 2018b).
535
536 **Molecular dynamics simulation**
537 We used the all-atom model for SXT17TM utilizing initial structures predicted by
538 trRosetta, a method based on deep learning (*Du et al.*, 2021). Because five different
539 three-dimensional structural models were predicted (TM score > 0.7), each was used in
540 the simulations. The lipid bilayer was modeled using the HMMM model, which was
541 developed to study protein–membrane interactions more efficiently by replacing the
542 membrane lipids with short-chain lipid and organic solvents to facilitate lateral diffusion
543 (*Ohkubo et al.*, 2012). The lipid headgroups in the HMMM model were identical to
544 those in the all-atom model and faithfully represented the membrane surface. The lipid
545 membrane consisted of 300 lipid molecules in each leaflet. The membranes with and
546 without PI4P were examined for lipid compositions of POPC:POPE:POPI4P (POPI14)
547 = 70:20:10 or 70:30:0, respectively. The initial configuration was prepared so that the
548 center of mass of STX17TM was located 3 nm above the membrane surface and the
549 first principal axis of the atomic configuration was tilted 45 degrees from the z axis. The
550 protein and lipids were solvated in a 10 nm × 10 nm × 30 nm box with the TIP3P water
551 model and 0.15 M KCl ions. The initial configurations were built by the Membrane
552 Builder module in the CHARMM-GUI server (*Jo et al.*, 2008). All molecular dynamics
553 simulations were performed using GENESIS (*Jung et al.*, 2015). The CHARMM36
554 force-field was used to describe the interactions in the system (*Huang et al.*, 2017).
555 Energy minimization was performed for 1000 steps by the steepest descent algorithm

556 and then by the conjugate gradient algorithm. Then, a 250 ps NVT simulation was
557 performed at 303.15 K for solvent equilibration, followed by a 1.6 ns NPT equilibration
558 to 1 atm using the Langevin thermostat/barostat (*Quigley and Probert*, 2004). The
559 production simulations were performed for 100 ns with a time-step of 2.5 fs and the
560 Langevin thermostat/barostat. Long-range electrostatic interactions were simulated
561 using the particle-mesh Ewald method (*Darden et al.*, 1993; *Essmann et al.*, 1995). The
562 short-range electrostatic and van der Waals interactions both used a cutoff of 12 Å. All
563 bonds were constrained by the SHAKE/RATTLE algorithm (*Andersen*, 1983; *Ryckaert*
564 *et al.*, 1977).
565
566 **Statistical analysis**
567 Comparisons between data from two groups were evaluated using Welch's *t*-test, and
568 comparisons of data among multiple groups were performed using one-way analysis of
569 variance (ANOVA) followed by the Dunnett's, Sidak's, or Tukey's multiple comparison
570 tests as implemented in GraphPad Prism 8 and 9 (GraphPad Software). Data
571 distributions were assumed to be normal, but this was not formally tested.
572
573 **Acknowledgments**
574 We thank Shoji Yamaoka for providing pMRX-IP vector, Teruhito Yasui for the pCG-
575 gag-pol and pCG-VSV-G vectors, Hiroyuki Arai for *C. elegans* cDNA and GFP–
576 Evectin-2, Masayuki Miura for *D. melanogaster* cDNA, Tamas Balla for GFP–PKD
577 C1ab, Harald Stenmark for mRFP–2xFYVE, Yuji Sugita and Ai Niitsu for helpful
578 discussions on the molecular dynamics calculations, and Koki Kamiya and Shoji
579 Takeuchi for helping the liposome experiments. The numerical computations were
580 performed with the RIKEN supercomputer system (HOKUSAI). We thank Eisuke
581 Itakura for technical advice on the *in vitro* experiments. We thank the members of the
582 Mizushima Laboratory for helpful discussions, especially Maya Shirakawa for technical
583 assistance with the experiments. This work was supported by Grants-in-Aid for
584 Specially Promoted Research (22H04919 to N.M.), for Transformative Research Areas
585 (A) (21H05256 to H.Y.), for Scientific Research (C) (23K05715 to Y.S.), and for JSPS
586 Fellows (17J02747 to S.S.) from the Japan Society for the Promotion of Science (JSPS)

and by the Exploratory Research for Advanced Technology (ERATO) research funding program of the Japan Science and Technology Agency (JST) (JPMJER1702 to N.M.).

Author Contributions

S.S., H.Y., and N.M. designed the project and analyzed the data. S.S. performed most experimental work and analyzed data. Y.S. designed, performed, and analyzed the molecular dynamics simulation. S.S., T.M., M.U., and H.Y. performed *in vitro* reconstitution experiments. S.S., I.K.H., J.S., and H.Y. performed *in vivo* PI4P depletion analysis. S.S., Y.S., H.Y., and N.M. wrote the manuscript. H.Y. and N.M. supervised the project. All authors commented on the manuscript.

Competing Interest

Noboru Mizushima: a Reviewing editor, *eLife*. The other authors declare that no competing interests exist.

603 **References**

604

605 Allen, E.A., C. Amato, T.M. Fortier, P. Velentzas, W. Wood, and E.H. Baehrecke. 2020.
606 A conserved myotubularin-related phosphatase regulates autophagy by
607 maintaining autophagic flux. *J. Cell Biol.* **219**:e201909073. doi:
608 10.1083/jcb.201909073, PMID: 32915229
609 Andersen, H.C. 1983. Rattle: A "velocity" version of the shake algorithm for molecular
610 dynamics calculations. *J. Comput. Phys.* **52**:24-34. doi: 10.1016/0021-
611 9991(83)90014-1, PMID:
612 Balla, A., G. Tuymetova, A. Tsiomenko, P. Varnai, and T. Balla. 2005. A plasma
613 membrane pool of phosphatidylinositol 4-phosphate is generated by
614 phosphatidylinositol 4-kinase type-III alpha: studies with the PH domains of the
615 oxysterol binding protein and FAPP1. *Mol. Biol. Cell*. **16**:1282-1295. doi:
616 10.1091/mbc.e04-07-0578, PMID: 15635101
617 Balla, T. 2013. Phosphoinositides: tiny lipids with giant impact on cell regulation.
618 *Physiol. Rev.* **93**:1019-1137. doi: 10.1152/physrev.00028.2012, PMID: 23899561
619 Baraldi, E., K. Djinovic Carugo, M. Hyvonen, P.L. Surdo, A.M. Riley, B.V. Potter, R.
620 O'Brien, J.E. Ladbury, and M. Saraste. 1999. Structure of the PH domain from
621 Bruton's tyrosine kinase in complex with inositol 1,3,4,5-tetrakisphosphate.
622 *Structure*. **7**:449-460. doi: 10.1016/s0969-2126(99)80057-4, PMID: 10196129
623 Barbosa, I.C., H. Shikata, M. Zourelidou, M. Heilmann, I. Heilmann, and C.
624 Schwechheimer. 2016. Phospholipid composition and a polybasic motif
625 determine D6 PROTEIN KINASE polar association with the plasma membrane
626 and tropic responses. *Development*. **143**:4687-4700. doi: 10.1242/dev.137117,
627 PMID: 27836964
628 Barz, S., F. Kriegenburg, A. Henning, A. Bhattacharya, H. Mancilla, P. Sanchez-Martin,
629 and C. Kraft. 2020. Atg1 kinase regulates autophagosome-vacuole fusion by
630 controlling SNARE bundling. *EMBO Rep.* **21**:e51869. doi:
631 10.15252/embr.202051869, PMID: 33274589
632 Bigay, J., and B. Antonny. 2012. Curvature, lipid packing, and electrostatics of
633 membrane organelles: defining cellular territories in determining specificity.
634 *Dev. Cell*. **23**:886-895. doi: 10.1016/j.devcel.2012.10.009, PMID: 23153485
635 Borgese, N., I. Gazzoni, M. Barberi, S. Colombo, and E. Pedrazzini. 2001. Targeting of
636 a tail-anchored protein to endoplasmic reticulum and mitochondrial outer
637 membrane by independent but competing pathways. *Mol. Biol. Cell*. **12**:2482-
638 2496. doi: 10.1091/mbc.12.8.2482, PMID: 11514630

639 Carlton, J.G., and P.J. Cullen. 2005. Coincidence detection in phosphoinositide
640 signaling. *Trends Cell Biol.* **15**:540-547. doi: 10.1016/j.tcb.2005.08.005, PMID:
641 16139503
642 Cebollero, E., A. van der Vaart, M. Zhao, E. Rieter, D.J. Klionsky, J.B. Helms, and F.
643 Reggiori. 2012. Phosphatidylinositol-3-phosphate clearance plays a key role in
644 autophagosome completion. *Curr. Biol.* **22**:1545-1553. doi:
645 10.1016/j.cub.2012.06.029, PMID: 22771041
646 Chen, J., and Z.J. Chen. 2018. PtdIns4P on dispersed trans-Golgi network mediates
647 NLRP3 inflammasome activation. *Nature*. **564**:71-76. doi: 10.1038/s41586-018-
648 0761-3, PMID: 30487600
649 Darden, T., D. York, and L. Pedersen. 1993. Particle mesh Ewald: An $N \cdot \log(N)$ method
650 for Ewald sums in large systems. *J. Chem. Phys.* **98**:10089-10092. doi:
651 10.1063/1.464397, PMID:
652 Dong, W., X. Zhang, W. Liu, Y.J. Chen, J. Huang, E. Austin, A.M. Celotto, W.Z. Jiang,
653 M.J. Palladino, Y. Jiang, G.R. Hammond, and Y. Hong. 2015. A conserved
654 polybasic domain mediates plasma membrane targeting of Lgl and its regulation
655 by hypoxia. *J. Cell Biol.* **211**:273-286. doi: 10.1083/jcb.201503067, PMID:
656 26483556
657 Dong, X.P., D. Shen, X. Wang, T. Dawson, X. Li, Q. Zhang, X. Cheng, Y. Zhang, L.S.
658 Weisman, M. Delling, and H. Xu. 2010. PI(3,5)P_2 controls membrane trafficking
659 by direct activation of mucolipin Ca^{2+} release channels in the endolysosome.
660 *Nat. Commun.* **1**:38. doi: 10.1038/ncomms1037, PMID: 20802798
661 Dowler, S., R.A. Currie, D.G. Campbell, M. Deak, G. Kular, C.P. Downes, and D.R.
662 Alessi. 2000. Identification of pleckstrin-homology-domain-containing proteins
663 with novel phosphoinositide-binding specificities. *Biochem. J.* **351**:19-31. doi:
664 10.1042/0264-6021:3510019, PMID: 11001876
665 Du, Z., H. Su, W. Wang, L. Ye, H. Wei, Z. Peng, I. Anishchenko, D. Baker, and J. Yang.
666 2021. The trRosetta server for fast and accurate protein structure prediction. *Nat.*
667 *Protoc.* **16**:5634-5651. doi: 10.1038/s41596-021-00628-9, PMID: 34759384
668 Essmann, U., L. Perera, M.L. Berkowitz, T. Darden, H. Lee, and L.G. Pedersen. 1995. A
669 smooth particle mesh Ewald method. *J. Chem. Phys.* **103**:8577-8593. doi:
670 10.1063/1.470117, PMID:
671 Gao, J., R. Kurre, J. Rose, S. Walter, F. Frohlich, J. Piehler, F. Reggiori, and C.
672 Ungermann. 2020. Function of the SNARE Ykt6 on autophagosomes requires
673 the Dsl1 complex and the Atg1 kinase complex. *EMBO Rep.* **21**:e50733. doi:
674 10.15252/embr.202050733, PMID: 33025734

675 Gozani, O., P. Karuman, D.R. Jones, D. Ivanov, J. Cha, A.A. Lugovskoy, C.L. Baird, H.
676 Zhu, S.J. Field, S.L. Lessnick, J. Villasenor, B. Mehrotra, J. Chen, V.R. Rao, J.S.
677 Brugge, C.G. Ferguson, B. Payrastre, D.G. Myszka, L.C. Cantley, G. Wagner, N.
678 Divecha, G.D. Prestwich, and J. Yuan. 2003. The PHD finger of the chromatin-
679 associated protein ING2 functions as a nuclear phosphoinositide receptor. *Cell*.
680 **114**:99-111. doi: 10.1016/s0092-8674(03)00480-x, PMID: 12859901
681 Guo, B., Q. Liang, L. Li, Z. Hu, F. Wu, P. Zhang, Y. Ma, B. Zhao, A.L. Kovacs, Z.
682 Zhang, D. Feng, S. Chen, and H. Zhang. 2014. O-GlcNAc-modification of
683 SNAP-29 regulates autophagosome maturation. *Nat. Cell Biol.* **16**:1215-1226.
684 doi: 10.1038/ncb3066, PMID: 25419848
685 Hammond, G.R., M.J. Fischer, K.E. Anderson, J. Holdich, A. Koteci, T. Balla, and R.F.
686 Irvine. 2012. PI4P and PI(4,5)P_2 are essential but independent lipid determinants
687 of membrane identity. *Science*. **337**:727-730. doi: 10.1126/science.1222483,
688 PMID: 22722250
689 Hammond, G.R., M.P. Machner, and T. Balla. 2014. A novel probe for
690 phosphatidylinositol 4-phosphate reveals multiple pools beyond the Golgi. *J.*
691 *Cell Biol.* **205**:113-126. doi: 10.1083/jcb.201312072, PMID: 24711504
692 Hanada, K. 2006. Discovery of the molecular machinery CERT for endoplasmic
693 reticulum-to-Golgi trafficking of ceramide. *Mol. Cell. Biochem.* **286**:23-31. doi:
694 10.1007/s11010-005-9044-z, PMID: 16601923
695 Hara, T., A. Takamura, C. Kishi, S. Iemura, T. Natsume, J.L. Guan, and N. Mizushima.
696 2008. FIP200, a ULK-interacting protein, is required for autophagosome
697 formation in mammalian cells. *J. Cell Biol.* **181**:497-510. doi:
698 10.1083/jcb.200712064, PMID: 18443221
699 Heo, W.D., T. Inoue, W.S. Park, M.L. Kim, B.O. Park, T.J. Wandless, and T. Meyer.
700 2006. PI(3,4,5)P3 and PI(4,5)P2 lipids target proteins with polybasic clusters to
701 the plasma membrane. *Science*. **314**:1458-1461. doi: 10.1126/science.1134389,
702 PMID: 17095657
703 Horie, C., H. Suzuki, M. Sakaguchi, and K. Mihara. 2002. Characterization of signal
704 that directs C-tail-anchored proteins to mammalian mitochondrial outer
705 membrane. *Mol. Biol. Cell*. **13**:1615-1625. doi: 10.1091/mbc.01-12-0570,
706 PMID: 12006657
707 Huang, J., S. Rauscher, G. Nawrocki, T. Ran, M. Feig, B.L. de Groot, H. Grubmuller,
708 and A.D. MacKerell, Jr. 2017. CHARMM36m: an improved force field for
709 folded and intrinsically disordered proteins. *Nat. Methods*. **14**:71-73. doi:
710 10.1038/nmeth.4067, PMID: 27819658

711 Itakura, E., C. Kishi-Itakura, and N. Mizushima. 2012. The hairpin-type tail-anchored
712 SNARE syntaxin 17 targets to autophagosomes for fusion with
713 endosomes/lysosomes. *Cell*. **151**:1256-1269. doi: 10.1016/j.cell.2012.11.001,
714 PMID: 23217709
715 Jo, S., T. Kim, V.G. Iyer, and W. Im. 2008. CHARMM-GUI: a web-based graphical user
716 interface for CHARMM. *J. Comput. Chem.* **29**:1859-1865. doi:
717 10.1002/jcc.20945, PMID: 18351591
718 Judith, D., H.B.J. Jefferies, S. Boeing, D. Frith, A.P. Snijders, and S.A. Tooze. 2019.
719 ATG9A shapes the forming autophagosome through Arfaptin 2 and
720 phosphatidylinositol 4-kinase IIIβ. *J. Cell Biol.* **218**:1634-1652. doi:
721 10.1083/jcb.201901115, PMID: 30917996
722 Jung, J., T. Mori, C. Kobayashi, Y. Matsunaga, T. Yoda, M. Feig, and Y. Sugita. 2015.
723 GENESIS: a hybrid-parallel and multi-scale molecular dynamics simulator with
724 enhanced sampling algorithms for biomolecular and cellular simulations. *Wiley*
725 *Interdiscip. Rev. Comput. Mol. Sci.* **5**:310-323. doi: 10.1002/wcms.1220, PMID:
726 26753008
727 Kabeya, Y., N. Mizushima, T. Ueno, A. Yamamoto, T. Kirisako, T. Noda, E. Kominami,
728 Y. Ohsumi, and T. Yoshimori. 2000. LC3, a mammalian homologue of yeast
729 Apg8p, is localized in autophagosome membranes after processing. *EMBO J.*
730 **19**:5720-5728. doi: 10.1093/emboj/19.21.5720, PMID: 11060023
731 Kassas, N., E. Tanguy, T. Thahouly, L. Fouillen, D. Heintz, S. Chasserot-Golaz, M.F.
732 Bader, N.J. Grant, and N. Vitale. 2017. Comparative characterization of
733 phosphatidic acid sensors and their localization during frustrated phagocytosis.
734 *J. Biol. Chem.* **292**:4266-4279. doi: 10.1074/jbc.M116.742346, PMID:
735 28115519
736 Kitamura, T., Y. Koshino, F. Shibata, T. Oki, H. Nakajima, T. Nosaka, and H. Kumagai.
737 2003. Retrovirus-mediated gene transfer and expression cloning: powerful tools
738 in functional genomics. *Exp. Hematol.* **31**:1007-1014. doi: S0301472X03002601
739 [pii], PMID: 14585362
740 Koyama-Honda, I., E. Itakura, T.K. Fujiwara, and N. Mizushima. 2013. Temporal
741 analysis of recruitment of mammalian ATG proteins to the autophagosome
742 formation site. *Autophagy*. **9**:1491-1499. doi: 10.4161/auto.25529, PMID:
743 23884233
744 Kumar, S., A. Jain, F. Farzam, J. Jia, Y. Gu, S.W. Choi, M.H. Mudd, A. Claude-Taupin,
745 M.J. Wester, K.A. Lidke, T.E. Rusten, and V. Deretic. 2018a. Mechanism of
746 Stx17 recruitment to autophagosomes via IRGM and mammalian Atg8 proteins.

747 *J. Cell Biol.* **217**:997-1013. doi: 10.1083/jcb.201708039, PMID: 29420192
748 Kumar, S., G. Stecher, M. Li, C. Knyaz, and K. Tamura. 2018b. MEGA X: Molecular
749 evolutionary genetics analysis across computing platforms. *Mol. Biol. Evol.*
750 **35**:1547-1549. doi: 10.1093/molbev/msy096, PMID: 29722887
751 Kurokawa, Y., A. Yoshida, E. Fujii, K. Tomioku, H. Hayashi, K. Tanabe, and A. Fujita.
752 2019. Phosphatidylinositol 4-phosphate on Rab7-positive autophagosomes
753 revealed by the freeze-fracture replica labeling. *Traffic*. **20**:82-95. doi:
754 10.1111/tra.12623, PMID: 30426618
755 Lemmon, M.A. 2008. Membrane recognition by phospholipid-binding domains. *Nat.*
756 *Rev. Mol. Cell Biol.* **9**:99-111. doi: 10.1038/nrm2328, PMID: 18216767
757 Levine, T.P., and S. Munro. 1998. The pleckstrin homology domain of oxysterol-
758 binding protein recognises a determinant specific to Golgi membranes. *Curr.*
759 *Biol.* **8**:729-739. doi: 10.1016/s0960-9822(98)70296-9, PMID: 9651677
760 Li, J., Z. Gao, D. Zhao, L. Zhang, X. Qiao, Y. Zhao, H. Ding, P. Zhang, J. Lu, J. Liu, H.
761 Jiang, C. Luo, and C. Chen. 2017. PI-273, a Substrate-Competitive, Specific
762 Small-Molecule Inhibitor of PI4KIIalpha, Inhibits the Growth of Breast Cancer
763 Cells. *Cancer Res.* **77**:6253-6266. doi: 10.1158/0008-5472.CAN-17-0484,
764 PMID: 28827373
765 Li, L., X. Shi, X. Guo, H. Li, and C. Xu. 2014. Ionic protein-lipid interaction at the
766 plasma membrane: what can the charge do? *Trends Biochem. Sci.* **39**:130-140.
767 doi: 10.1016/j.tibs.2014.01.002, PMID: 24534649
768 Liu, H., W. Shao, W. Liu, W. Shang, J.P. Liu, L. Wang, and C. Tong. 2023. PtdIns4P
769 exchange at endoplasmic reticulum-autolysosome contacts is essential for
770 autophagy and neuronal homeostasis. *Autophagy*:online ahead of print. doi:
771 10.1080/15548627.2023.2222556, PMID: 37289040
772 Lu, J., W. Dong, Y. Tao, and Y. Hong. 2021. Electrostatic plasma membrane targeting
773 contributes to Dlg function in cell polarity and tumorigenesis. *Development*.
774 **148**:dev196956. doi: 10.1242/dev.196956, PMID: 33688074
775 Manford, A., T. Xia, A.K. Saxena, C. Stefan, F. Hu, S.D. Emr, and Y. Mao. 2010.
776 Crystal structure of the yeast Sac1: implications for its phosphoinositide
777 phosphatase function. *EMBO J.* **29**:1489-1498. doi: 10.1038/emboj.2010.57,
778 PMID: 20389282
779 Matsui, T., P. Jiang, S. Nakano, Y. Sakamaki, H. Yamamoto, and N. Mizushima. 2018.
780 Autophagosomal YKT6 is required for fusion with lysosomes independently of
781 syntaxin 17. *J. Cell Biol.* **217**:2633-2645. doi: 10.1083/jcb.201712058, PMID:
782 29789439

783 Mizushima, N., and B. Levine. 2020. Autophagy in human diseases. *N. Engl. J. Med.*
784 **383**:1564-1576. doi: 10.1056/NEJMra2022774, PMID: 33053285
785 Moravcevic, K., C.L. Oxley, and M.A. Lemmon. 2012. Conditional peripheral
786 membrane proteins: facing up to limited specificity. *Structure*. **20**:15-27. doi:
787 10.1016/j.str.2011.11.012, PMID: 22193136
788 Morita, K., Y. Hama, T. Izume, N. Tamura, T. Ueno, Y. Yamashita, Y. Sakamaki, K.
789 Mimura, H. Morishita, W. Shihoya, O. Nureki, H. Mano, and N. Mizushima.
790 2018. Genome-wide CRISPR screen identifies TMEM41B as a gene required
791 for autophagosome formation. *J. Cell Biol.* **217**:3817-3828. doi:
792 10.1083/jcb.201804132, PMID: 30093494
793 Nguyen, T.N., B.S. Padman, J. Usher, V. Oorschot, G. Ramm, and M. Lazarou. 2016.
794 Atg8 family LC3/GABARAP proteins are crucial for autophagosome-lysosome
795 fusion but not autophagosome formation during PINK1/Parkin mitophagy and
796 starvation. *J. Cell Biol.* **215**:857-874. doi: 10.1083/jcb.201607039, PMID:
797 27864321
798 Ohkubo, Y.Z., T.V. Pogorelov, M.J. Arcario, G.A. Christensen, and E. Tajkhorshid.
799 2012. Accelerating membrane insertion of peripheral proteins with a novel
800 membrane mimetic model. *Biophys. J.* **102**:2130-2139. doi:
801 10.1016/j.bpj.2012.03.015, PMID: 22824277
802 Platre, M.P., and Y. Jaillais. 2016. Guidelines for the Use of Protein Domains in Acidic
803 Phospholipid Imaging. *Methods Mol. Biol*. **1376**:175-194. doi: 10.1007/978-1-
804 4939-3170-5_15, PMID: 26552684
805 Platre, M.P., L.C. Noack, M. Doumane, V. Bayle, M.L.A. Simon, L. Maneta-Peyret, L.
806 Fouillen, T. Stanislas, L. Armengot, P. Pejchar, M.C. Caillaud, M. Potocky, A.
807 Copic, P. Moreau, and Y. Jaillais. 2018. A combinatorial lipid code shapes the
808 electrostatic landscape of plant endomembranes. *Dev. Cell*. **45**:465-480 e411.
809 doi: 10.1016/j.devcel.2018.04.011, PMID: 29754803
810 Quigley, D., and M.I. Probert. 2004. Langevin dynamics in constant pressure extended
811 systems. *J. Chem. Phys.* **120**:11432-11441. doi: 10.1063/1.1755657, PMID:
812 15268177
813 Rao, M., V. Okreglak, U.S. Chio, H. Cho, P. Walter, and S.O. Shan. 2016. Multiple
814 selection filters ensure accurate tail-anchored membrane protein targeting. *eLife*.
815 **5**:e21301. doi: 10.7554/eLife.21301, PMID: 27925580
816 Reuter, L., T. Schmidt, P. Manishankar, C. Throm, J. Keicher, A. Bock, I. Droste-Borel,
817 and C. Oecking. 2021. Light-triggered and phosphorylation-dependent 14-3-3
818 association with NON-PHOTOTROPIC HYPOCOTYL 3 is required for

hypocotyl phototropism. *Nat. Commun.* **12**:6128. doi: 10.1038/s41467-021-26332-6, PMID: 34675219

Ryckaert, J.-P., G. Ciccotti, and H.J.C. Berendsen. 1977. Numerical integration of the cartesian equations of motion of a system with constraints: molecular dynamics of n-alkanes. *J. Comput. Phys.* **23**:327-341. doi: 10.1016/0021-9991(77)90098-5, PMID:

Saitoh, T., H. Nakano, N. Yamamoto, and S. Yamaoka. 2002. Lymphotoxin-β receptor mediates NEMO-independent NF-κB activation. *FEBS Lett.* **532**:45-51. doi: 10.1016/s0014-5793(02)03622-0, PMID: 12459460

Sanchez-Martin, P., F. Kriegenburg, L. Alves, J. Adam, J. Elsaesser, R. Babic, H. Mancilla, M. Licheva, G. Tascher, C. Munch, S. Eimer, and C. Kraft. 2023. ULK1-mediated phosphorylation regulates the conserved role of YKT6 in autophagy. *J. Cell Sci.* **136**:jcs260546. doi: 10.1242/jcs.260546, PMID: 36644903

Schink, K.O., K.W. Tan, and H. Stenmark. 2016. Phosphoinositides in Control of Membrane Dynamics. *Annu. Rev. Cell Dev. Biol.* **32**:143-171. doi: 10.1146/annurev-cellbio-111315-125349, PMID: 27576122

Sengupta, N., M. Jovic, E. Barnaeva, D.W. Kim, X. Hu, N. Southall, M. Dejmek, I. Mejdrova, R. Nencka, A. Baumlova, D. Chalupska, E. Boura, M. Ferrer, J. Marugan, and T. Balla. 2019. A large scale high-throughput screen identifies chemical inhibitors of phosphatidylinositol 4-kinase type II alpha. *J. Lipid Res.* **60**:683-693. doi: 10.1194/jlr.D090159, PMID: 30626625

Sharma, A., M. Mariappan, S. Appathurai, and R.S. Hegde. 2010. In vitro dissection of protein translocation into the mammalian endoplasmic reticulum. *Methods Mol. Biol*. **619**:339-363. doi: 10.1007/978-1-60327-412-8_20, PMID: 20419420

Simon, M.L., M.P. Platre, M.M. Marques-Bueno, L. Armengot, T. Stanislas, V. Bayle, M.C. Caillaud, and Y. Jaillais. 2016. A PtdIns(4)P-driven electrostatic field controls cell membrane identity and signalling in plants. *Nat. Plants*. **2**:16089. doi: 10.1038/nplants.2016.89, PMID: 27322096

Soreng, K., T.P. Neufeld, and A. Simonsen. 2018. Membrane trafficking in autophagy. *Int. Rev. Cell. Mol. Biol*. **336**:1-92. doi: 10.1016/bs.ircmb.2017.07.001, PMID: 29413888

Synek, L., R. Pleskot, J. Sekeres, N. Serrano, N. Vukasinovic, J. Ortmannova, M. Klejchova, P. Pejchar, K. Batystova, M. Gutkowska, E. Jankova-Drdova, V. Markovic, T. Pecenkova, J. Santrucek, V. Zarsky, and M. Potocky. 2021. Plasma membrane phospholipid signature recruits the plant exocyst complex via the

855 EXO70A1 subunit. *Proc. Natl. Acad. Sci. U. S. A.* **118**:e2105287118. doi:
856 10.1073/pnas.2105287118, PMID: 34470819
857 Taguchi-Atarashi, N., M. Hamasaki, K. Matsunaga, H. Omori, N.T. Ktistakis, T.
858 Yoshimori, and T. Noda. 2010. Modulation of local PtdIns3P levels by the PI
859 phosphatase MTMR3 regulates constitutive autophagy. *Traffic*. **11**:468-478. doi:
860 10.1111/j.1600-0854.2010.01034.x, PMID: 20059746
861 Takáts, S., P. Nagy, A. Varga, K. Pircs, M. Kárpáti, K. Varga, A.L. Kovács, K. Hegedűs,
862 and G. Juhász. 2013. Autophagosomal Syntaxin17-dependent lysosomal
863 degradation maintains neuronal function in *Drosophila*. *J. Cell Biol.* **201**:531-
864 539. doi: 10.1083/jcb.201211160, PMID: 23671310
865 Tsuboyama, K., I. Koyama-Honda, Y. Sakamaki, M. Koike, H. Morishita, and N.
866 Mizushima. 2016. The ATG conjugation systems are important for degradation
867 of the inner autophagosomal membrane. *Science*. **354**:1036-1041. doi:
868 10.1126/science.aaf6136, PMID: 27885029
869 van der Schaar, H.M., P. Leyssen, H.J. Thibaut, A. de Palma, L. van der Linden, K.H.
870 Lanke, C. Lacroix, E. Verbeken, K. Conrath, A.M. Macleod, D.R. Mitchell, N.J.
871 Palmer, H. van de Poel, M. Andrews, J. Neyts, and F.J. van Kuppeveld. 2013. A
872 novel, broad-spectrum inhibitor of enterovirus replication that targets host cell
873 factor phosphatidylinositol 4-kinase IIIbeta. *Antimicrob. Agents Chemother.*
874 **57**:4971-4981. doi: 10.1128/AAC.01175-13, PMID: 23896472
875 Varnai, P., and T. Balla. 1998. Visualization of phosphoinositides that bind pleckstrin
876 homology domains: calcium- and agonist-induced dynamic changes and
877 relationship to myo-[3H]inositol-labeled phosphoinositide pools. *J. Cell Biol.*
878 **143**:501-510. doi: 10.1083/jcb.143.2.501, PMID: 9786958
879 Wang, H., H.Q. Sun, X. Zhu, L. Zhang, J. Albanesi, B. Levine, and H. Yin. 2015.
880 GABARAPs regulate PI4P-dependent autophagosome:lysosome fusion. *Proc.*
881 *Natl. Acad. Sci. U. S. A.* **112**:7015-7020. doi: 10.1073/pnas.1507263112, PMID:
882 26038556
883 Wang, Y., H. Que, C. Li, Z. Wu, F. Jian, Y. Zhao, H. Tang, Y. Chen, S. Gao, C.C.L.
884 Wong, Y. Li, C. Zhao, and Y. Rong. 2023. ULK phosphorylation of STX17
885 controls autophagosome maturation via FLNA. *J. Cell Biol.* **222**:e202211025.
886 doi: 10.1083/jcb.202211025, PMID: 37389864
887 Yagita, Y., T. Hiromasa, and Y. Fujiki. 2013. Tail-anchored PEX26 targets peroxisomes
888 via a PEX19-dependent and TRC40-independent class I pathway. *J. Cell Biol.*
889 **200**:651-666. doi: 10.1083/jcb.201211077, PMID: 23460677
890 Yesbolatova, A., Y. Saito, N. Kitamoto, H. Makino-Itou, R. Ajima, R. Nakano, H.

Nakaoka, K. Fukui, K. Gamo, Y. Tominari, H. Takeuchi, Y. Saga, K.I. Hayashi, and M.T. Kanemaki. 2020. The auxin-inducible degron 2 technology provides sharp degradation control in yeast, mammalian cells, and mice. *Nat. Commun.* **11**:5701. doi: 10.1038/s41467-020-19532-z, PMID: 33177522

Yeung, T., G.E. Gilbert, J. Shi, J. Silvius, A. Kapus, and S. Grinstein. 2008. Membrane phosphatidylserine regulates surface charge and protein localization. *Science*. **319**:210-213. doi: 10.1126/science.1152066, PMID: 18187657

Yeung, T., and S. Grinstein. 2007. Lipid signaling and the modulation of surface charge during phagocytosis. *Immunol. Rev.* **219**:17-36. doi: 10.1111/j.1600-065X.2007.00546.x, PMID: 17850479

Yeung, T., M. Terebiznik, L. Yu, J. Silvius, W.M. Abidi, M. Philips, T. Levine, A. Kapus, and S. Grinstein. 2006. Receptor activation alters inner surface potential during phagocytosis. *Science*. **313**:347-351. doi: 10.1126/science.1129551, PMID: 16857939

906 **Figure legends**

907

908 **Figure 1.** The recruitment of STX17 to autophagosomes is dependent on its positively
909 charged C-terminal region.
910 (A) Schematic representation of the structures of STX17 and its C-terminal variants.
911 The positively (orange) and negatively (blue) charged residues are shown. Alanine
912 substitutions are shown in green. TMH, transmembrane helix; CTR, C-terminal region.
913 (B) Schematic representation of the localization of ATG5, LC3B, and STX17 during
914 autophagosome formation and maturation.
915 (C–E) Mouse embryonic fibroblasts (MEFs) stably expressing mRuby3-LC3B and
916 GFP–STX17TM (containing the two transmembrane helices and the C-terminal region)
917 or its mutants were cultured in starvation medium for 1 h. Bars indicate 10 μm (main
918 images) and 1 μm (insets). Quantification of GFP–STX17TM intensity of mRuby3–
919 LC3B-positive ring-like structures ($n > 30$) are shown in the graphs. Solid horizontal
920 lines indicate medians, boxes indicate the interquartile ranges (25th to 75th percentiles),
921 and whiskers indicate the 5th to 95th percentiles. Differences were statistically analyzed
922 by Welch's *t*-test (C) or one-way ANOVA followed by Dunnett's multiple comparison
923 test (D and E).

924

925 **Figure 2.** Autophagosomes become negatively charged during maturation.
926 (A) GFP–STX17TM translated *in vitro* was incubated with rhodamine-labeled
927 liposomes containing the indicated concentrations of phospholipids: 70%
928 phosphatidylcholine (PC), 20% phosphatidylethanolamine (PE), and 10% of either PE,
929 phosphatidylserine (PS), phosphatidylinositol 3-phosphate (PI3P), or
930 phosphatidylinositol 4-phosphate (PI4P). Bars indicate 1 μm. GFP intensities of
931 liposomes are quantified and shown as in Figure 1C ($n > 30$).
932 (B) Amino acid sequences of GFP-tagged membrane surface charge probes. The
933 positively charged residues are shown in orange. The farnesylation motif is indicated in
934 green.
935 (C and D) Mouse embryonic fibroblasts (MEFs) stably expressing one of the GFP-
936 tagged charge probes and mRuby3-STX17TM (C) or mRuby3–LC3B (D) were cultured

937 in starvation medium for 1 h. GFP intensities of mRuby3–STX17TM-positive (C) or
938 mRuby3–LC3B-positive (D) ring-like structures were quantified ($n > 70$).
939 (E and F) Time-lapse analysis of MEFs stably expressing the GFP-tagged 1K8Q (E) or
940 5K4Q (F) charge probes and mRuby3–STX17TM or mRuby3–LC3B cultured in
941 starvation medium. Autophagosomes are indicated by arrows. Bars indicate 1 μm.
942 (G) Summary of electrostatic dynamics of autophagosome formation.
943 Solid horizontal lines indicate medians, boxes indicate the interquartile ranges (25th to
944 75th percentiles), and whiskers indicate the 5th to 95th percentiles. Differences were
945 statistically analyzed by one-way ANOVA followed by Sidak's multiple comparison test
946 (A, C, and D).
947
948 **Figure 3.** Phosphatidylinositol 4-phosphate (PI4P) is enriched in the autophagosomal
949 membrane during maturation.
950 (A) Mouse embryonic fibroblasts (MEFs) stably expressing GFP–CERT(PHD) and
951 mRuby3–STX17TM or mRuby3–ATG5 were cultured in starvation medium for 1 h.
952 Bars indicate 10 μm (main images) and 1 μm (insets). GFP intensities of mRuby3-
953 positive structures ($n > 60$) were quantified. Solid horizontal lines indicate medians,
954 boxes indicate the interquartile ranges (25th to 75th percentiles), and whiskers indicate
955 the 5th to 95th percentiles. Differences were statistically analyzed by Welch's *t*-test.
956 (B–D) Time-lapse analysis of MEFs stably expressing GFP–CERT(PHD) and mRuby3–
957 ATG5 (B), WIPI2B–mRuby3 (C), or mRuby3–STX17TM and HaloTag7–LC3B
958 (visualized with SaraFluor 650T HaloTag ligand) (D) cultured in starvation medium.
959 Autophagosomes are indicated by arrows. Bars indicate 1 μm.
960
961 **Figure 4.** STX17 recruitment to autophagosomes depends on phosphatidylinositol 4-
962 phosphate (PI4P) *in vitro*.
963 (A) Schematic representation of the *in vitro* autophagosome recruitment assay. Isolated
964 autophagosomes were mixed with mGFP–STX17TM and either recombinant Sac1-
965 phosphatase domain (Sac1PD) or its phosphatase-dead mutant (C392S).
966 (B) Isolation of mature autophagosomes prior to their fusion with lysosomes.
967 Homogenates of *STX17* knockout HeLa cells stably expressing mRuby3–LC3B cultured

968 in starvation medium at 1 h were separated by the OptiPrep membrane flotation method.
969 The autophagosome-containing fraction (#1: LC3-positive and LAMP1-negative) was
970 collected. The positions of mRuby3–LC3B (black arrowhead) and endogenous LC3B
971 (white arrowhead) are indicated.
972 (C) Purification of recombinant yeast Sac1 (phosphatase domain, PD) and its
973 phosphatase-dead (C392S) mutant and mGFP–STX17TM from High Five cells.
974 (D) *In vitro* autophagosome association assay. Isolated autophagosomes were mixed
975 with recombinant Sac1 (WT or C392S) for 30 min and then with mGFP–STX17TM for
976 another 30 min. Representative images are shown. Bars indicate 2.5 μm. STX17-
977 positivity rates were determined across three independent experiments (two of the three
978 experiments were performed in a blind manner, and 80 autophagosomes were counted
979 in each experiment). Solid horizontal lines indicate means. Differences were statistically
980 analyzed by one-way ANOVA followed by Tukey's test.
981
982 **Figure 5.** Molecular dynamics simulations of phosphatidylinositol 4-phosphate (PI4P-
983 dependent STX17TM insertion into membranes.
984 (A and C) An example of a time series of simulated results of STX17TM insertion into a
985 membrane consisting of 70% phosphatidylcholine (PC), 20% phosphatidylethanolamine
986 (PE), and 10% PI4P (POPI14) (A) or 70% PC and 30% PE (C). STX17TM is shown in
987 blue. Phosphorus in POPC, POPE, and PI4P are indicated by yellow, cyan, and red,
988 respectively. Short-tailed lipids are represented as green sticks. The time evolution
989 series of (A) is shown in Video 1.
990 (B and D) Time evolution of the z-coordinate of the center of mass (z_{cm}) of the
991 transmembrane helices of STX17TM in the case of membranes with (B) and without
992 (D) PI4P. Five independent simulation results are represented by solid lines of different
993 colors. The gray dashed lines indicate the locations of the lipid heads. The time
994 evolution series of (B) is shown in Video 2.
995 (E) Model of the PI4P-driven electrostatic maturation of the autophagosome and STX17
996 recruitment.
997
998 **Figure 1—figure supplement 1.** Recruitment of STX17 depends on the abundance of

999 cationic amino acids in the C-terminal region but not on its specific amino acid
1000 sequence.
1001 (A) Multiple sequence alignment of STX17 proteins from *Homo sapiens* (Hs), *Mus*
1002 *musculus*, *Danio rerio*, *Ciona intestinalis*, *Drosophila melanogaster* (Dm), and
1003 *Caenorhabditis elegans* (Ce). Identical residues between more than two species are
1004 indicated with gray boxes. Domains of STX17 are indicated with different colors: green,
1005 the Habc domain; magenta, the SNARE domain; blue, transmembrane helix (TMH);
1006 orange, a linker between the TMDs; and purple, the C-terminal region.
1007 (B) Mouse embryonic fibroblasts (MEFs) stably expressing mRuby3–LC3B and either
1008 GFP-tagged HsSTX17TM, DsSTX17TM, or CeSTX17TM were cultured in starvation
1009 medium for 1 h. GFP–STX17TM intensities of mRuby3–LC3B-positive ring-like
1010 structures were quantified ($n > 30$). Solid horizontal lines indicate medians, boxes
1011 indicate the interquartile ranges (25th to 75th percentiles), and whiskers indicate the 5th
1012 to 95th percentiles.
1013 (C) MEFs stably expressing one of the GFP-tagged alanine replacement mutants (shown
1014 in Figure 1A) and mRuby3–LC3B were cultured in starvation medium for 1 h.
1015 Quantification results are shown in Figure 1D. Bars indicate 10 μm (main images) and 1
1016 μm (insets).
1017 (D) MEFs stably expressing one of the GFP-tagged charge replacement mutants (shown
1018 in Figure 1E) and mRuby3–LC3B were cultured in starvation medium for 1 h.
1019 Quantification results are shown in Figure 1E. Bars indicate 10 μm (main images) and 1
1020 μm (insets).
1021
1022 **Figure 2—figure supplement 1.** Autophagosomes become negatively charged during
1023 maturation.
1024 (A) Mouse embryonic fibroblasts stably expressing one of the GFP-tagged charge
1025 probes and mRuby3–LC3B were cultured in starvation medium for 1 h. Bars indicate 10
1026 μm (main images) and 1 μm (insets).
1027 (B) Time-lapse analysis of MEFs stably expressing GFP–3K6Q and mRuby3–
1028 STX17TM or mRuby3–LC3B cultured in starvation medium. Autophagosomes are
1029 indicated by arrows. Bars indicate 1 μm.

1030 (C) Time-lapse analysis of MEFs stably expressing one of the GFP-tagged charge
1031 probes and mRuby3–ATG5 cultured in starvation medium. Autophagosomes are
1032 indicated by arrows. Bars indicate 1 μm.
1033
1034 **Figure 3—figure supplement 1.** Localization of phospholipids in mature
1035 autophagosomes.
1036 (A) Mouse embryonic fibroblasts (MEFs) stably expressing the indicated GFP-tagged
1037 phospholipid probe and mRuby3–STX17TM were cultured in starvation medium for 1
1038 h. The following phospholipid probes were used: phosphatidic acid (PA),
1039 Spo20(PABD); PS, Evectin-2; diacylglycerol (DAG), PKD C1ab; PI3P, 2×FYVE; PI4P,
1040 CERT(PHD); PI5P, ING2(PlantHD); PI(3,4)P_2, TAPP1(PHD); PI(4,5)P_2, PLCd1(PHD);
1041 PI(3,5)P_2, TRPML1(PHD); and PIP_3, Btk(PHD). Bars indicate 10 μm (main images)
1042 and 1 μm (insets).
1043 (B) MEFs stably expressing GFP–CERT(PHD) or TRPML1(PHD) were cultured in
1044 starvation medium containing LysoTracker Deep Red for 1 h. Bars indicate 10 μm
1045 (main images) and 1 μm (insets).
1046 (C) MEFs stably expressing GFP–PI4KB or GFP–PI4K2A were cultured in starvation
1047 medium for 1 h. Bars, 10 μm (main images) and 1 μm (insets).
1048
1049 **Figure 3—figure supplement 2.** Phosphatidylinositol 4-phosphate (PI4P) is enriched in
1050 mature autophagosomes before fusion with lysosomes.
1051 (A and B) Mouse embryonic fibroblasts (MEFs) stably expressing the indicated GFP-
1052 tagged indicated PI4P probe, FAPP(PHD), OSBP(PHD) or P4M-SidMx2, and mRuby3–
1053 STX17TM or mRuby3–ATG5 were cultured in starvation medium for 1 h. Bars indicate
1054 10 μm (main images) and 1 μm (insets) (A). GFP intensities of mRuby3-positive
1055 structures ($n > 50$) were quantified (B). Solid horizontal lines indicate medians, boxes
1056 indicate the interquartile ranges (25th to 75th percentiles), and whiskers indicate the 5th
1057 to 95th percentiles. Differences were statistically analyzed by Welch's *t*-test.
1058 (C) Time-lapse analysis of MEFs stably expressing GFP–CERT(PHD) cultured in
1059 starvation medium containing LysoTracker Deep Red. Bars indicate 1 μm.
1060 (D) U2OS cells stably expressing GFP–CERT(PHD) and mRuby3–LC3B were

1061 transfected with siSTX17 and siYKT6. After 3 days, cells were cultured in starvation
1062 medium for 1 h, and immunostained with anti-LAMP1 antibodies. Bars indicate 10 μm
1063 (main images) and 1 μm (insets).
1064
1065 **Video 1.** Molecular dynamics simulations of STX17TM insertion into a
1066 phosphatidylinositol 4-phosphate (PI4P)-containing membrane.
1067 STX17TM is shown in blue. Phosphorus in POPC (70%), POPE (20%), and PI4P (10%)
1068 are indicated by yellow, cyan, and red spheres, respectively. Short-tailed lipids are
1069 represented by green sticks. This video corresponds to Figure 5A.
1070
1071 **Video 2.** Molecular dynamics simulations of STX17TM insertion into a membrane
1072 without phosphatidylinositol 4-phosphate (PI4P).
1073 STX17TM is shown in blue. Phosphorus in POPC (70%) and POPE (30%) are indicated
1074 in yellow and cyan, respectively. Short-tailed lipids are represented by green sticks. This
1075 video corresponds to Figure 5B.

Figure 1

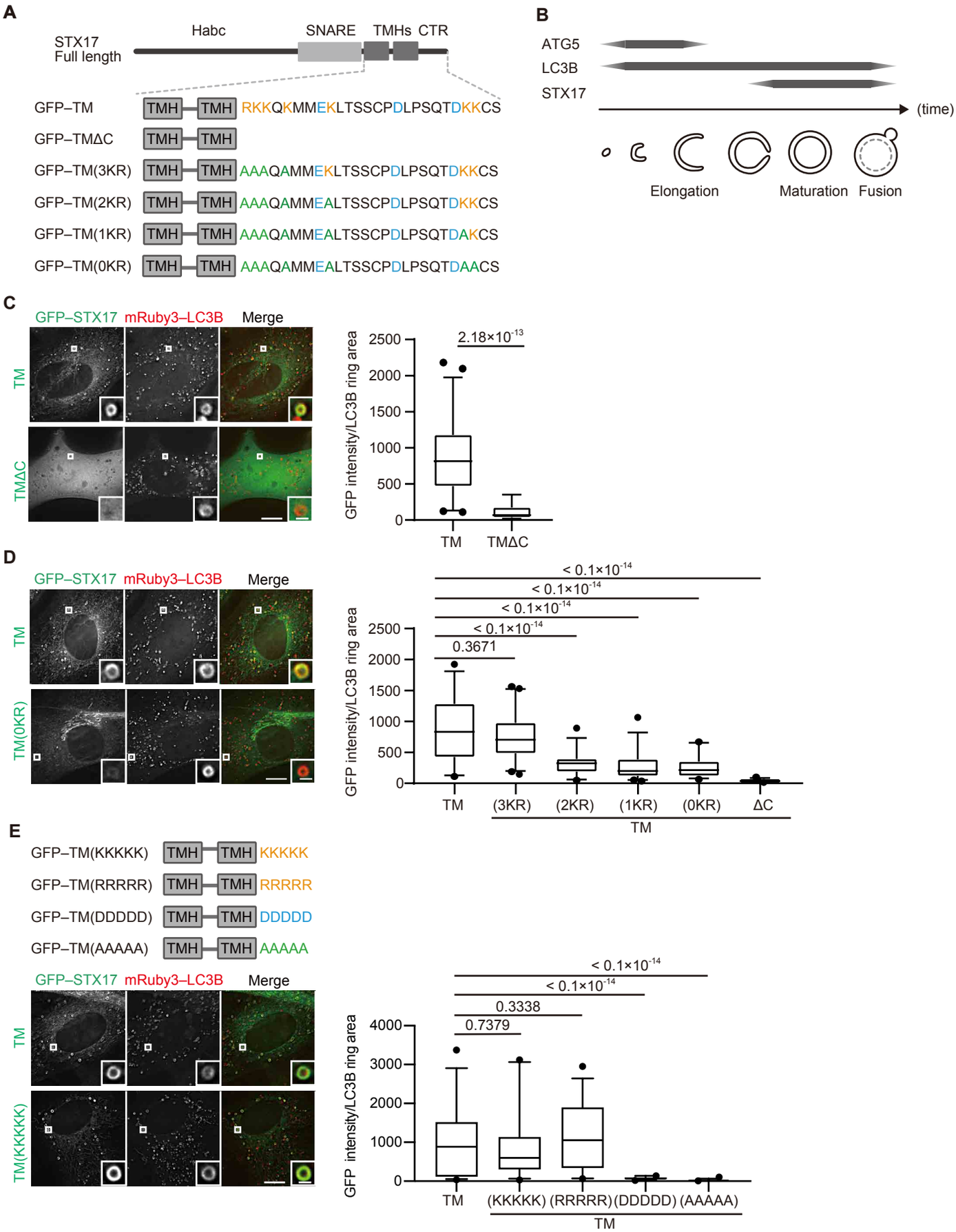

Figure 1. The recruitment of STX17 to autophagosomes is dependent on its positively charged C-terminal region
(A) Schematic representation of the structures of STX17 and its C-terminal variants. The positively (orange) and negatively (blue) charged residues are shown. Alanine substitutions are shown in green. TMH, transmembrane helix; CTR, C-terminal region.
(B) Schematic representation of the localization of ATG5, LC3B, and STX17 during autophagosome formation and maturation.
(C–E) Mouse embryonic fibroblasts (MEFs) stably expressing mRuby3-LC3B and GFP–STX17TM (containing the two transmembrane helices and the C-terminal region) or its mutants were cultured in starvation medium for 1 h. Bars indicate 10 μm (main images) and 1 μm (insets). Quantification of GFP–STX17TM intensity of mRuby3–LC3B-positive ring-like structures (n > 30) are shown in the graphs. Solid horizontal lines indicate medians, boxes indicate the interquartile ranges (25th to 75th percentiles), and whiskers indicate the 5th to 95th percentiles. Differences were statistically analyzed by Welch' s *t*-test (C) or one-way ANOVA followed by Dunnett' s multiple comparison test (D and E).

Figure 1−figure supplement 1

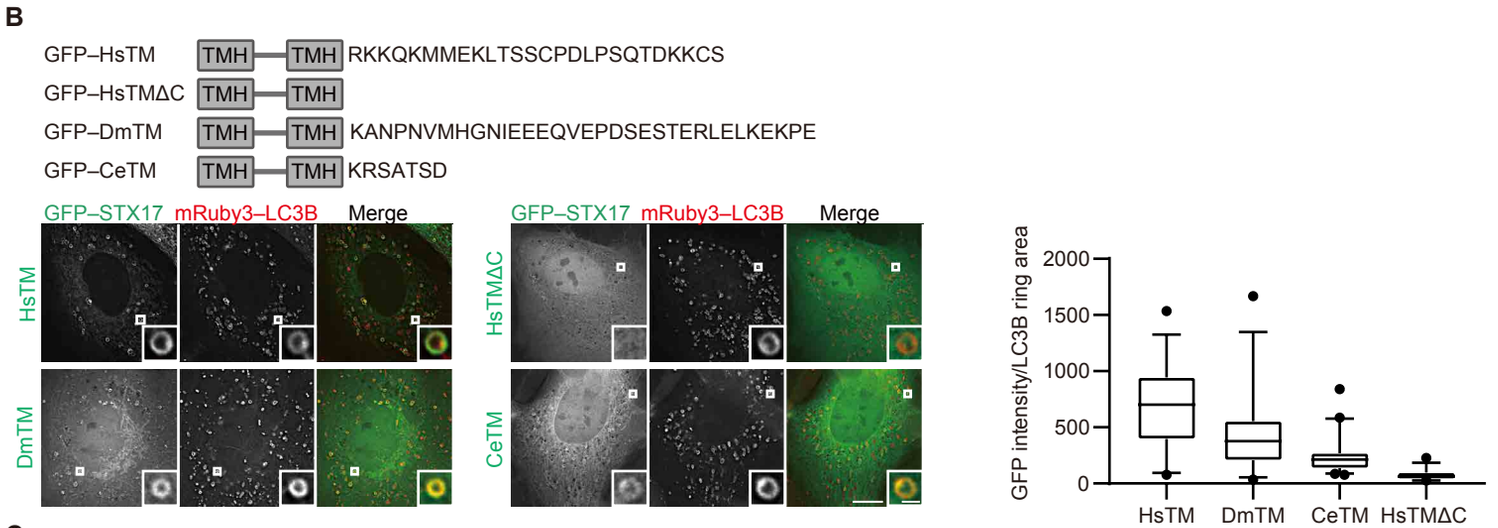

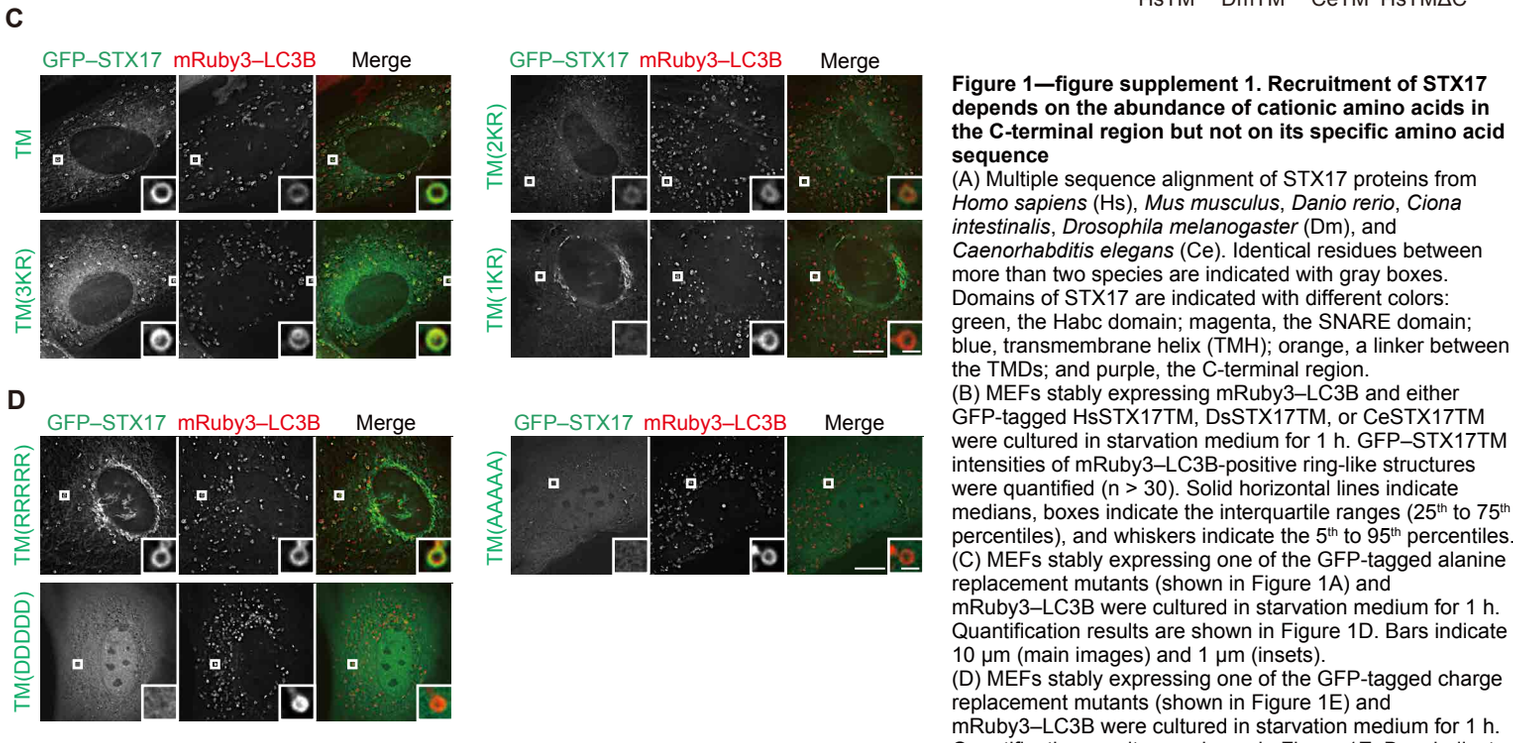

Figure 1—figure supplement 1. Recruitment of STX17 depends on the abundance of cationic amino acids in the C-terminal region but not on its specific amino acid sequence

(A) Multiple sequence alignment of STX17 proteins from *Homo sapiens* (Hs), *Mus musculus*, *Danio rerio*, *Ciona intestinalis*, *Drosophila melanogaster* (Dm), and *Caenorhabditis elegans* (Ce). Identical residues between more than two species are indicated with gray boxes. Domains of STX17 are indicated with different colors: green, the Habc domain; magenta, the SNARE domain; blue, transmembrane helix (TMH); orange, a linker between the TMDs; and purple, the C-terminal region.

(B) MEFs stably expressing mRuby3–LC3B and either GFP-tagged HsSTX17TM, DsSTX17TM, or CeSTX17TM were cultured in starvation medium for 1 h. GFP–STX17TM intensities of mRuby3–LC3B-positive ring-like structures were quantified (n > 30). Solid horizontal lines indicate medians, boxes indicate the interquartile ranges (25th to 75th percentiles), and whiskers indicate the 5th to 95th percentiles.

(C) MEFs stably expressing one of the GFP-tagged alanine replacement mutants (shown in Figure 1A) and mRuby3–LC3B were cultured in starvation medium for 1 h. Quantification results are shown in Figure 1D. Bars indicate 10 μm (main images) and 1 μm (insets).

(D) MEFs stably expressing one of the GFP-tagged charge replacement mutants (shown in Figure 1E) and mRuby3–LC3B were cultured in starvation medium for 1 h. Quantification results are shown in Figure 1E. Bars indicate 10 μm (main images) and 1 μm (insets).

Figure 2

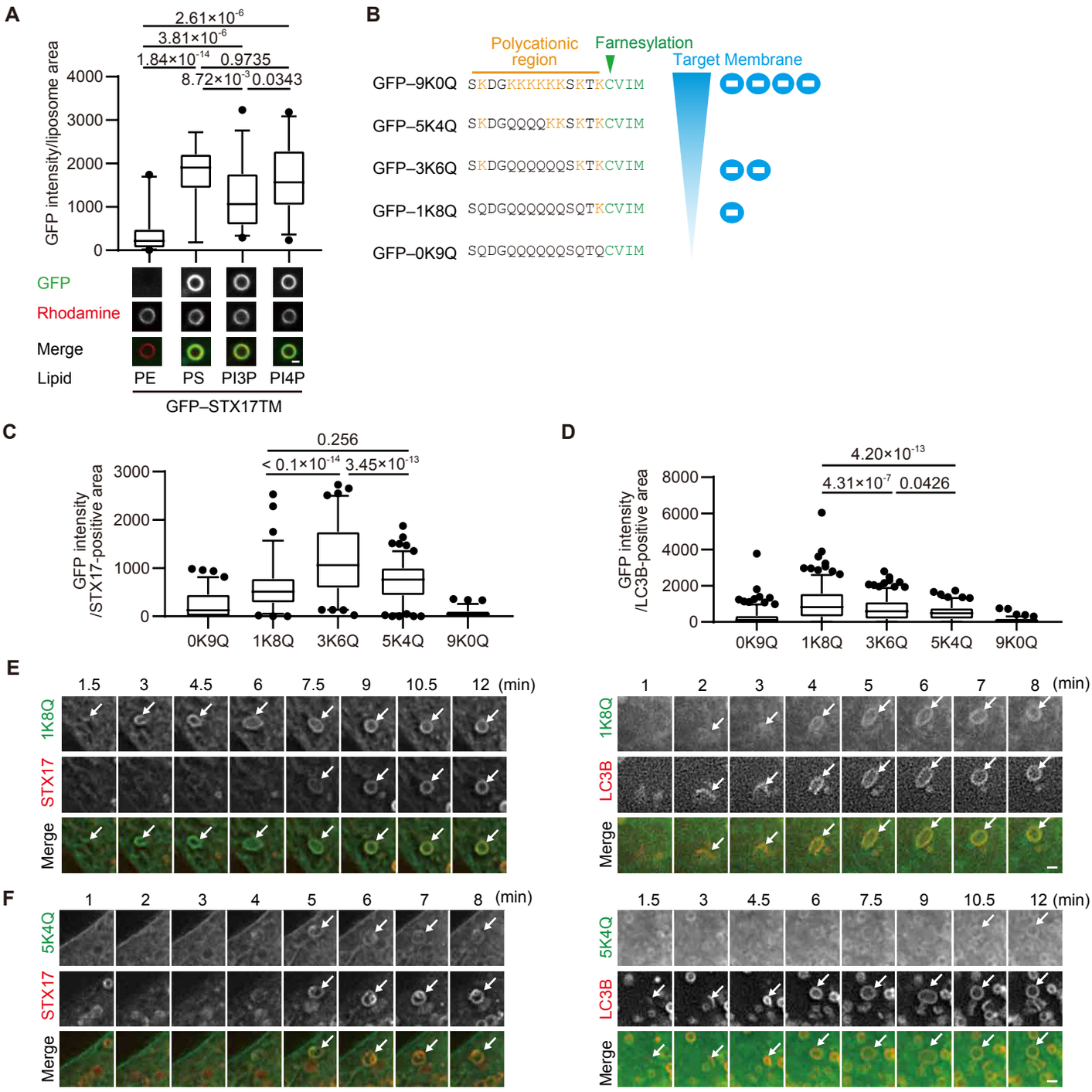

Figure 2. Autophagosomes become negatively charged during maturation

(A) GFP–STX17TM translated *in vitro* was incubated with rhodamine-labeled liposomes containing the indicated concentrations of phospholipids: 70% phosphatidylcholine (PC), 20% phosphatidylethanolamine (PE), and 10% of either PE, phosphatidylserine (PS), phosphatidylinositol 3-phosphate (PI3P), or phosphatidylinositol 4-phosphate (PI4P). Bars indicate 1 μm. GFP intensities of liposomes are quantified and shown as in Figure 1C (n > 30).

(B) Amino acid sequences of GFP-tagged membrane surface charge probes. The positively charged residues are shown in orange. The farnesylation motif is indicated in green.

(C and D) MEFs stably expressing one of the GFP-tagged charge probes and mRuby3-STX17TM (C) or mRuby3–LC3B (D) were cultured in starvation medium for 1 h. GFP intensities of mRuby3–STX17TM-positive (C) or mRuby3–LC3B-positive (D) ring-like structures were quantified (n > 70).

(E and F) Time-lapse analysis of MEFs stably expressing the GFP-tagged 1K8Q (E) or 5K4Q (F) charge probes and mRuby3–STX17TM or mRuby3–LC3B cultured in starvation medium. Autophagosomes are indicated by arrows. Bars indicate 1 μm.

(G) Summary of electrostatic dynamics of autophagosome formation.

Solid horizontal lines indicate medians, boxes indicate the interquartile ranges (25th to 75th percentiles), and whiskers indicate the 5th to 95th percentiles. Differences were statistically analyzed by one-way ANOVA followed by Sidak' s multiple comparison test (A, C, and D).

Figure 2−figure supplement 1

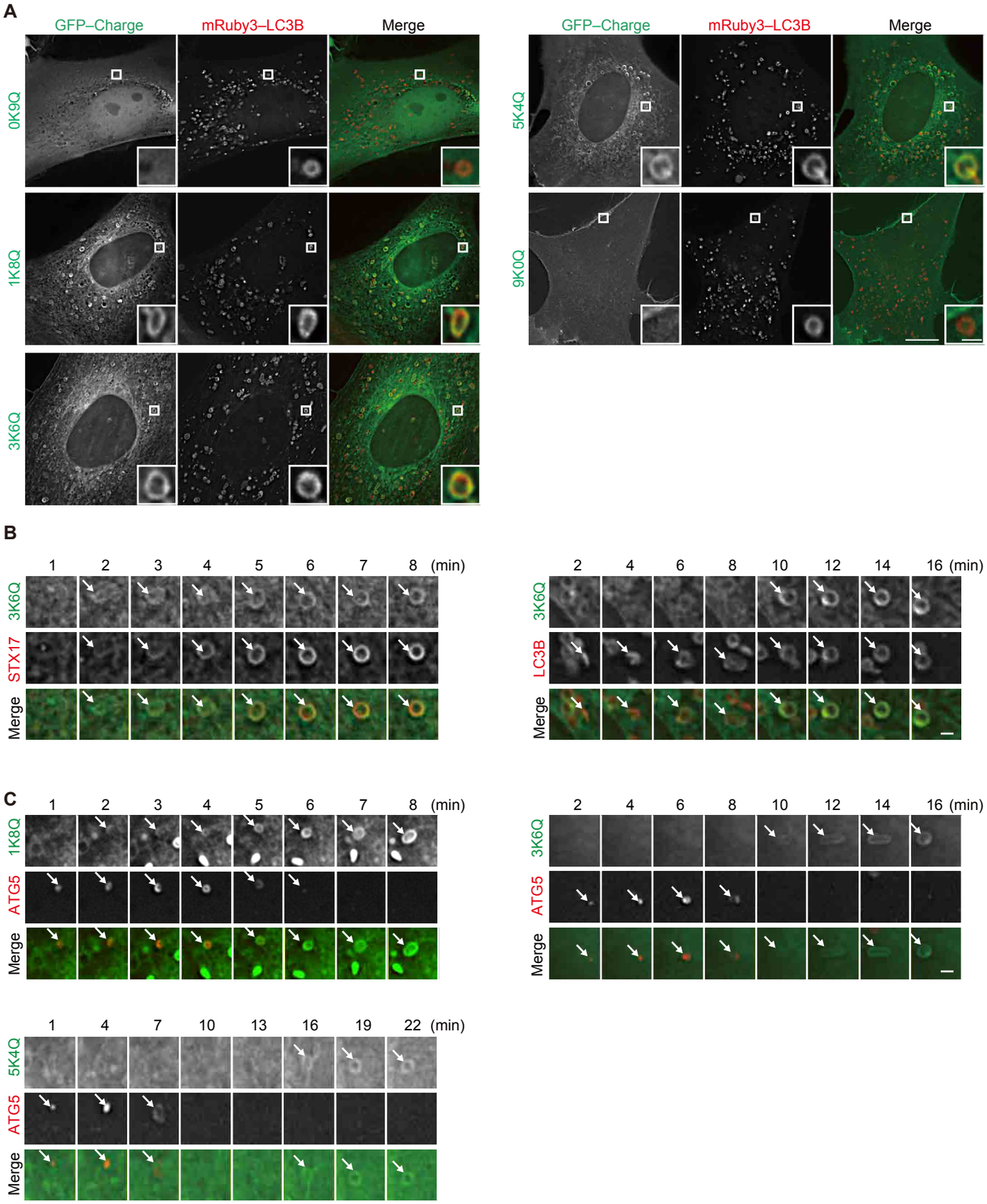

Figure 2—figure supplement 1. Autophagosomes become negatively charged during maturation
(A) MEFs stably expressing one of the GFP-tagged charge probes and mRuby3–LC3B were cultured in starvation medium for 1 h. Bars indicate 10 μm (main images) and 1 μm (insets).
(B) Time-lapse analysis of MEFs stably expressing GFP–3K6Q and mRuby3–STX17TM or mRuby3–LC3B cultured in starvation medium. Autophagosomes are indicated by arrows. Bars indicate 1 μm.
(C) Time-lapse analysis of MEFs stably expressing one of the GFP-tagged charge probes and mRuby3–ATG5 cultured in starvation medium. Autophagosomes are indicated by arrows. Bars indicate 1 μm.

Figure 3

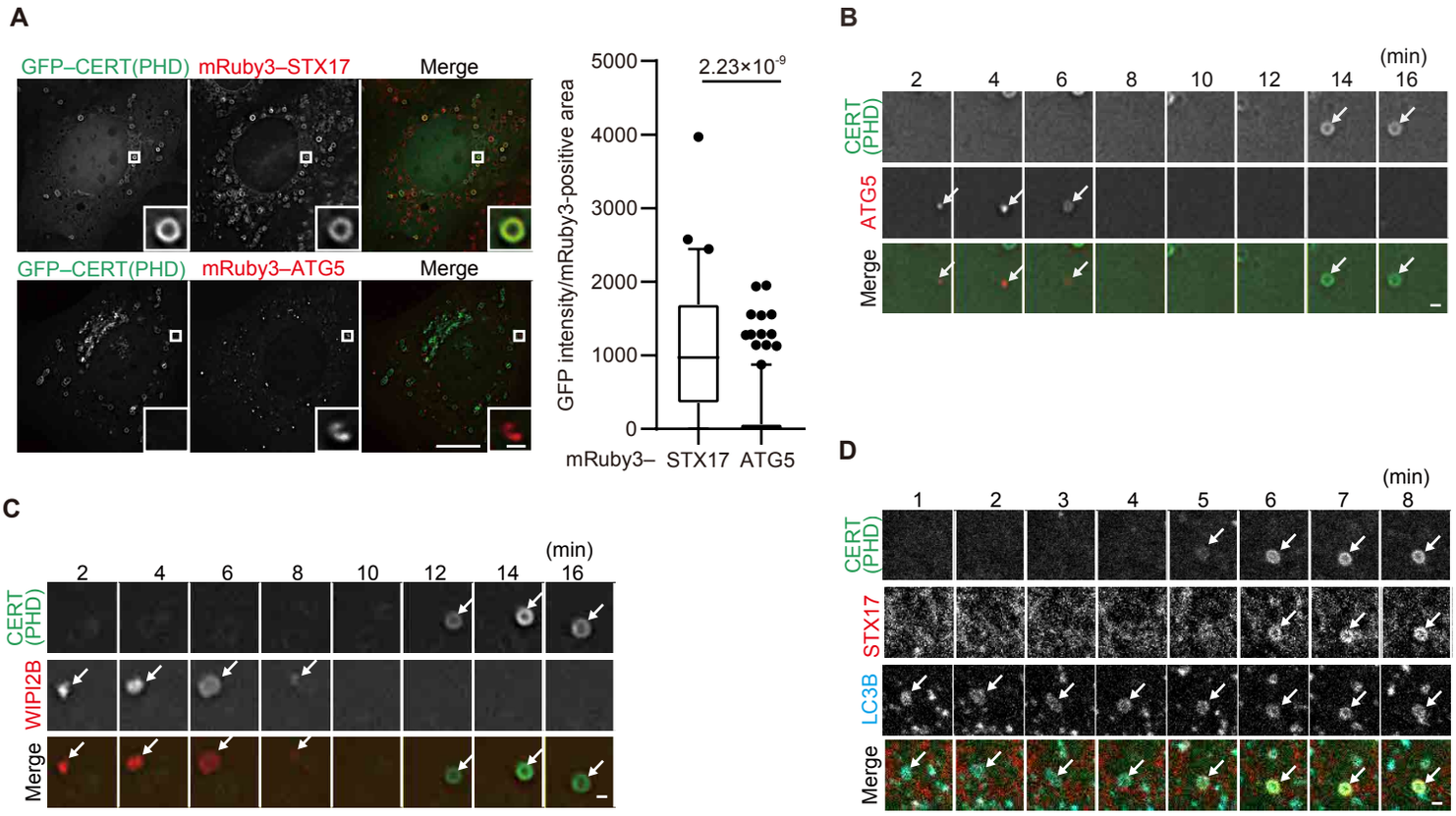

Figure 3. Phosphatidylinositol 4-phosphate (PI4P) is enriched in the autophagosomal membrane during maturation
(A) MEFs stably expressing GFP–CERT(PHD) and mRuby3–STX17TM or mRuby3–ATG5 were cultured in starvation medium for 1 h. Bars indicate 10 μm (main images) and 1 μm (insets). GFP intensities of mRuby3-positive structures (n > 60) were quantified. Solid horizontal lines indicate medians, boxes indicate the interquartile ranges (25th to 75th percentiles), and whiskers indicate the 5th to 95th percentiles. Differences were statistically analyzed by Welch' s *t*-test.
(B–D) Time-lapse analysis of MEFs stably expressing GFP–CERT(PHD) and mRuby3–ATG5 (B), WIPI2B–mRuby3 (C), or mRuby3–STX17TM and HaloTag7–LC3B (visualized with SaraFluor 650T HaloTag ligand) (D) cultured in starvation medium. Autophagosomes are indicated by arrows. Bars indicate 1 μm.

Figure 3−figure supplement 1

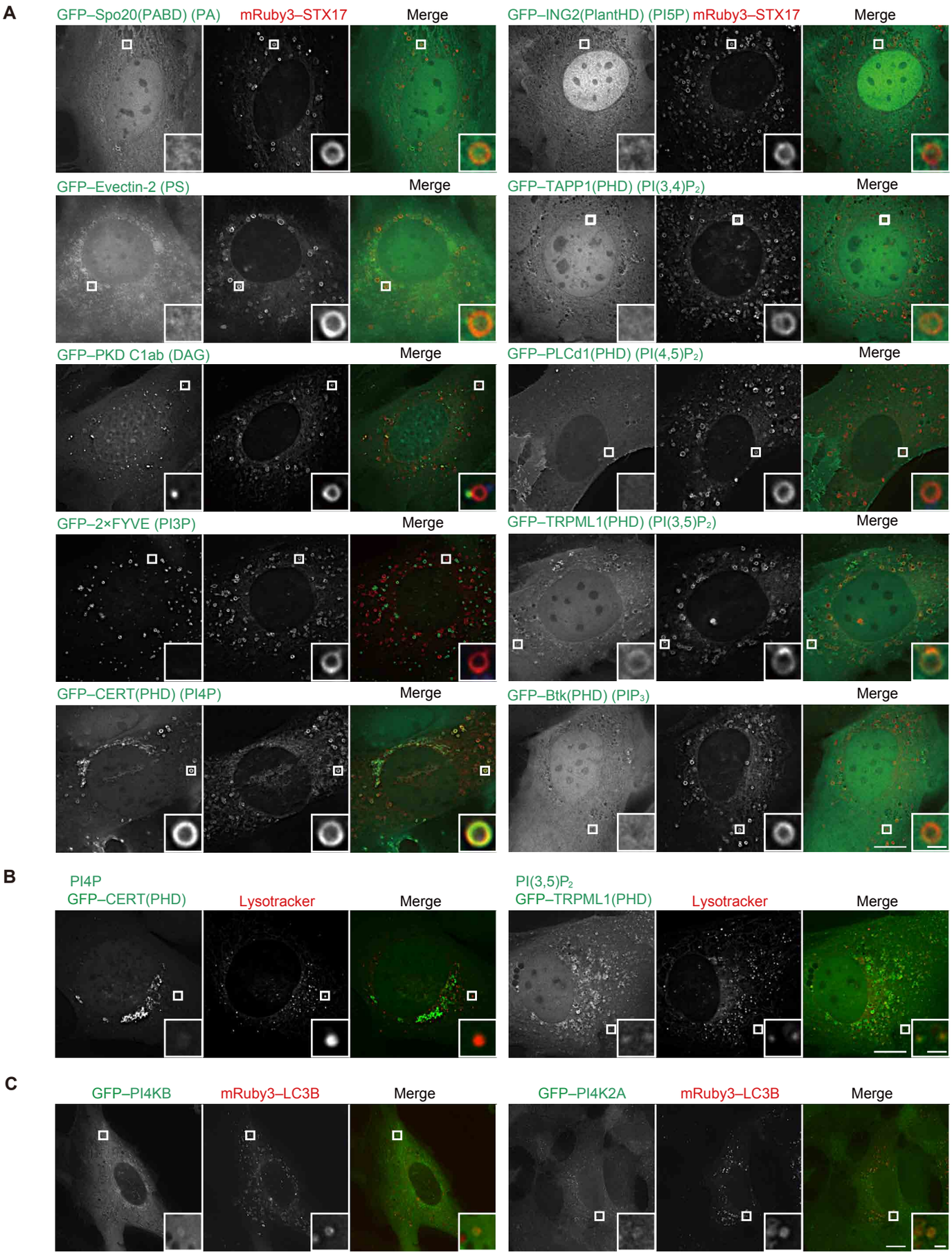

Figure 3—figure supplement 1. Localization of phospholipids in mature autophagosomes
(A) MEFs stably expressing the indicated GFP-tagged phospholipid probe and mRuby3–STX17TM were cultured in starvation medium for 1 h. The following phospholipid probes were used: phosphatidic acid (PA), Spo20(PABD); PS, Evectin-2; diacylglycerol (DAG), PKD C1ab; PI3P, 2×FYVE; PI4P, CERT(PHD); PI5P, ING2(PlantHD); PI(3,4)P2, TAPP1(PHD); PI(4,5)P2, PLCd1(PHD); PI(3,5)P2, TRPML1(PHD); and PIP3, Btk(PHD). Bars indicate 10 μm (main images) and 1 μm (insets).
(B) MEFs stably expressing GFP–CERT(PHD) or TRPML1(PHD) were cultured in starvation medium containing LysoTracker Deep Red for 1 h. Bars indicate 10 μm (main images) and 1 μm (insets).
(C) MEFs stably expressing GFP–PI4KB or GFP–PI4K2A were cultured in starvation medium for 1 h. Bars, 10 μm (main images) and 1 μm (insets).

Figure 3−figure supplement 2

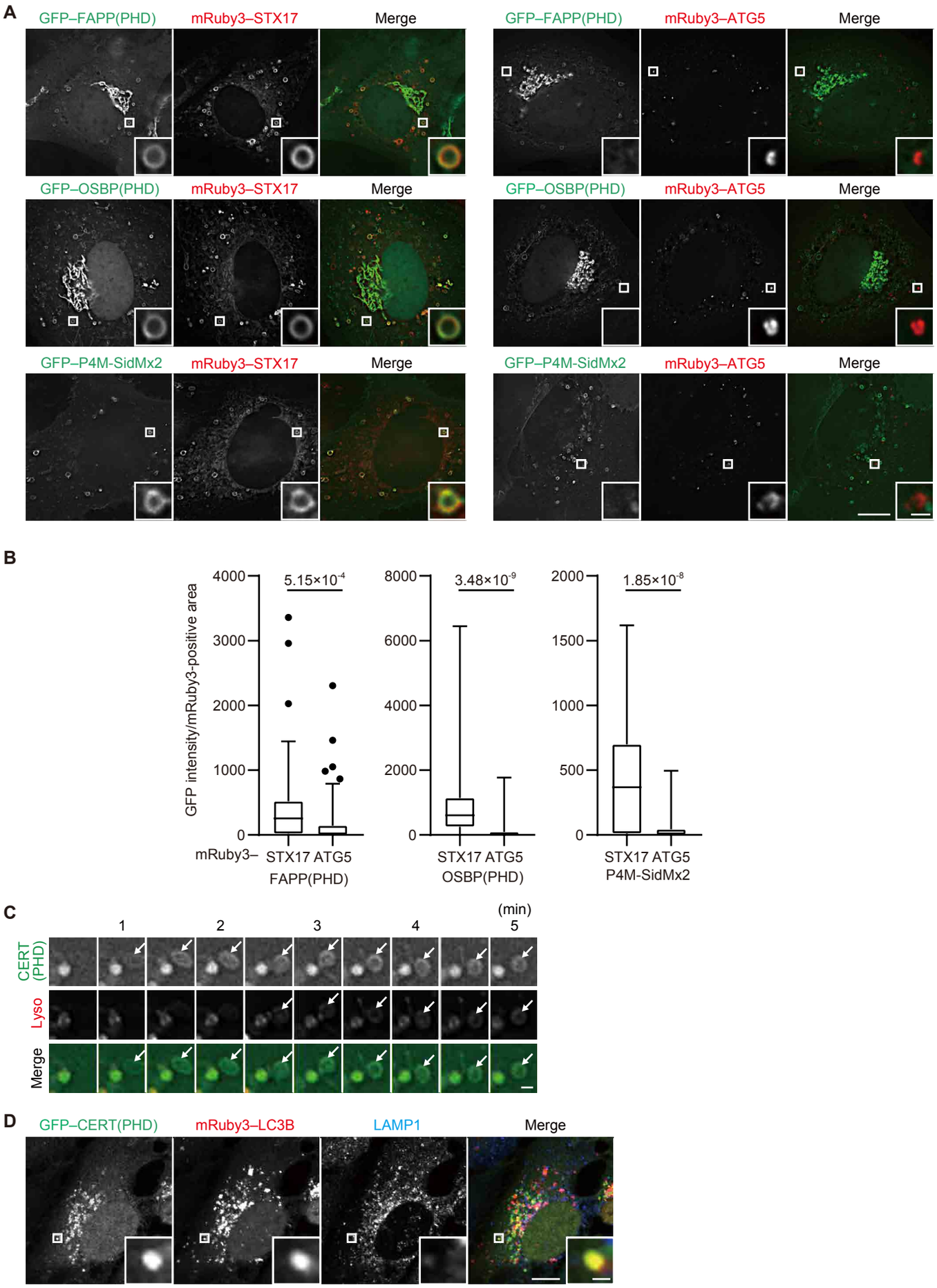

Figure 3—figure supplement 2. Phosphatidylinositol 4-phosphate (PI4P) is enriched in mature autophagosomes before fusion with lysosomes
(A and B) MEFs stably expressing the indicated GFP-tagged indicated PI4P probe, FAPP(PHD), OSBP(PHD) or P4M-SidMx2, and mRuby3–STX17TM or mRuby3–ATG5 were cultured in starvation medium for 1 h. Bars indicate 10 μm (main images) and 1 μm (insets) (A). GFP intensities of mRuby3-positive structures (n > 50) were quantified (B). Solid horizontal lines indicate medians, boxes indicate the interquartile ranges (25th to 75th percentiles), and whiskers indicate the 5th to 95th percentiles. Differences were statistically analyzed by Welch' s *t*-test.
(C) Time-lapse analysis of MEFs stably expressing GFP–CERT(PHD) cultured in starvation medium containing LysoTracker Deep Red. Bars indicate 1 μm.
(D) U2OS cells stably expressing GFP–CERT(PHD) and mRuby3–LC3B were transfected with siSTX17 and siYKT6. After 3 days, cells were cultured in starvation medium for 1 h, and immunostained with anti-LAMP1 antibodies. Bars indicate 10 μm (main images) and 1 μm (insets).

Figure 4

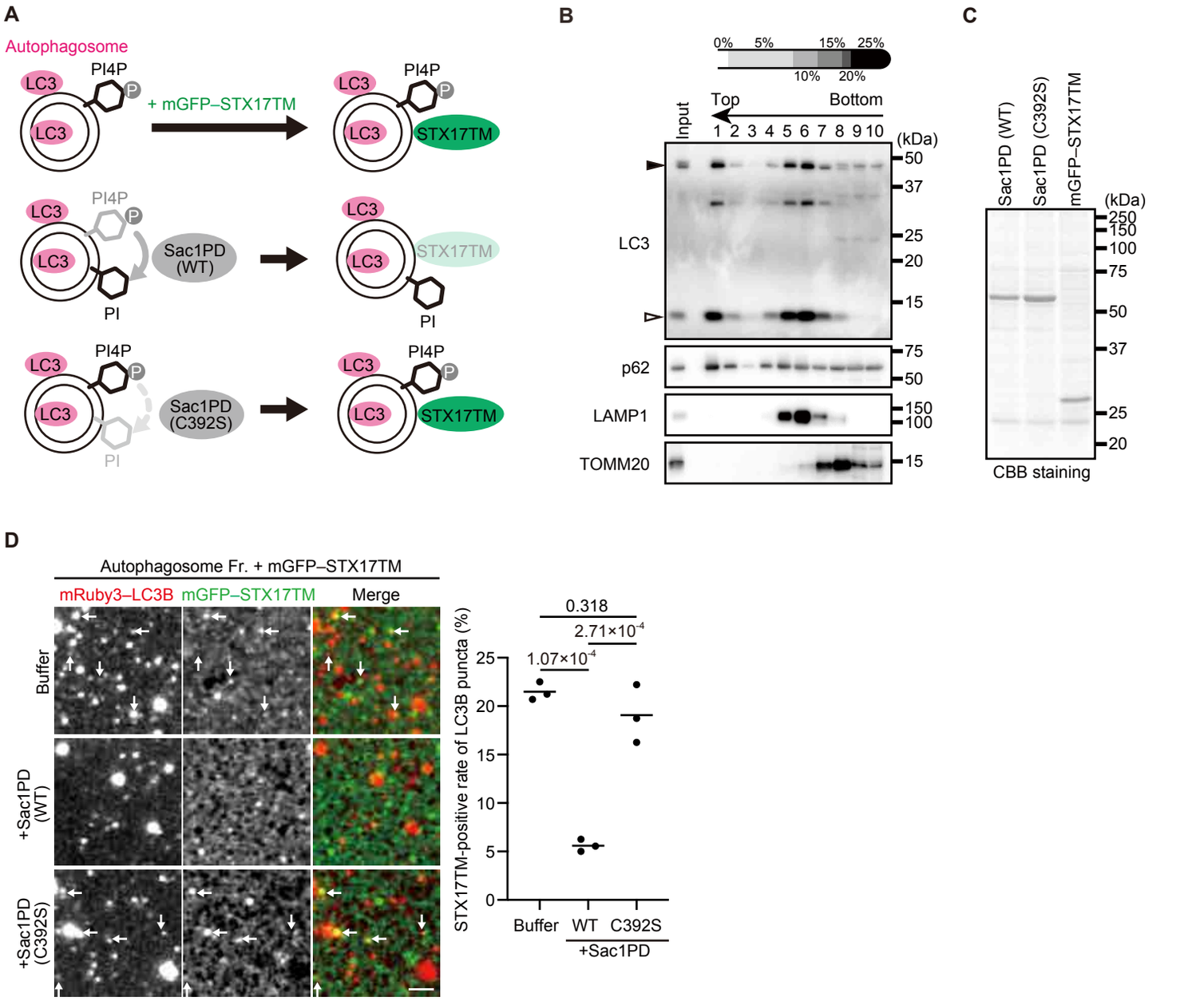

Figure 4. STX17 recruitment to autophagosomes depends on phosphatidylinositol 4-phosphate (PI4P) *in vitro*
(A) Schematic representation of the *in vitro* autophagosome recruitment assay. Isolated autophagosomes were mixed with mGFP–STX17TM and either recombinant Sac1-phosphatase domain (Sac1PD) or its phosphatase-dead mutant (C392S).
(B) Isolation of mature autophagosomes prior to their fusion with lysosomes. Homogenates of *STX17* knockout HeLa cells stably expressing mRuby3–LC3B cultured in starvation medium at 1 h were separated by the OptiPrep membrane flotation method. The autophagosome-containing fraction (#1: LC3-positive and LAMP1-negative) was collected. The positions of mRuby3–LC3B (black arrowhead) and endogenous LC3B (white arrowhead) are indicated.
(C) Purification of recombinant yeast Sac1 (phosphatase domain, PD) and its phosphatase-dead (C392S) mutant and mGFP–STX17TM from High Five cells.
(D) *In vitro* autophagosome association assay. Isolated autophagosomes were mixed with recombinant Sac1 (WT or C392S) for 30 min and then with mGFP–STX17TM for another 30 min. Representative images are shown. Bars indicate 2.5 μm. STX17-positivity rates were determined across three independent experiments (two of the three experiments were performed in a blind manner, and 80 autophagosomes were counted in each experiment). Solid horizontal lines indicate means. Differences were statistically analyzed by one-way ANOVA followed by Tukey' s test.

Figure 5

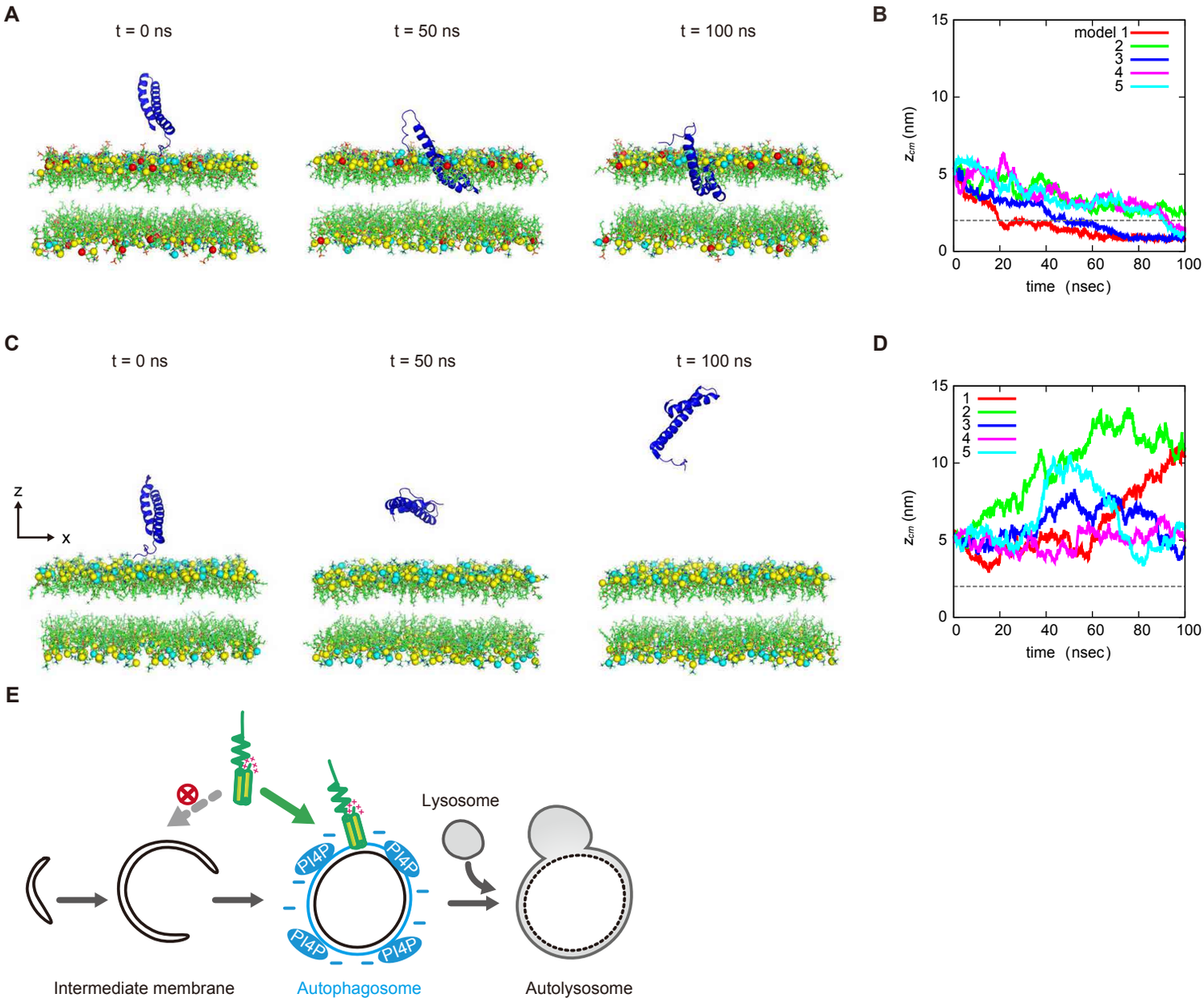

Figure 5. Molecular dynamics simulations of phosphatidylinositol 4-phosphate (PI4P-dependent STX17TM insertion into membranes
(A and C) An example of a time series of simulated results of STX17TM insertion into a membrane consisting of 70% phosphatidylcholine (PC), 20% phosphatidylethanolamine (PE), and 10% PI4P (POPI14) (A) or 70% PC and 30% PE (C). STX17TM is shown in blue. Phosphorus in POPC, POPE, and PI4P are indicated by yellow, cyan, and red, respectively. Short-tailed lipids are represented as green sticks. The time evolution series of (A) is shown in Video 1.
(B and D) Time evolution of the *z*-coordinate of the center of mass (z_{cm}) of the transmembrane helices of STX17TM in the case of membranes with (B) and without (D) PI4P. Five independent simulation results are represented by solid lines of different colors. The gray dashed lines indicate the locations of the lipid heads. The time evolution series of (B) is shown in Video 2.
(E) Model of the PI4P-driven electrostatic maturation of the autophagosome and STX17 recruitment.